



Contents lists available at ScienceDirect

## Journal of the Mechanics and Physics of Solids

journal homepage: [www.elsevier.com/locate/jmps](http://www.elsevier.com/locate/jmps)

## Topology optimization of flexoelectric structures

S.S. Nanthakumar<sup>c</sup>, Xiaoying Zhuang<sup>a,b,c,\*</sup>, Harold S. Park<sup>d,\*</sup>, Timon Rabczuk<sup>e,f,\*</sup><sup>a</sup> Department of Geotechnical Engineering, Tongji University, Shanghai, China<sup>b</sup> State Key Laboratory of Structural Analysis for Industrial Equipment, Dalian University of Technology, Dalian 116024, PR China<sup>c</sup> Institute of Continuum Mechanics, Leibniz University Hannover, Appelstrasse 11A, Hannover D-30167, Germany<sup>d</sup> Department of Mechanical Engineering, Boston University, 110 Cummington Mall, Boston MA 02215, Germany<sup>e</sup> Institute of Research and Development, Duy Tan University, 3 Quang Trung, Danang, Viet Nam<sup>f</sup> Institute of Structural Mechanics, Bauhaus-University Weimar, Marienstr. 15, Weimar D-99423, Germany

## ARTICLE INFO

## Article history:

Received 3 December 2016

Revised 17 May 2017

Accepted 17 May 2017

Available online 18 May 2017

## ABSTRACT

We present a mixed finite element formulation for flexoelectric nanostructures that is coupled with topology optimization to maximize their intrinsic material performance with regards to their energy conversion potential. Using Barium Titanate (BTO) as the model flexoelectric material, we demonstrate the significant enhancement in energy conversion that can be obtained using topology optimization. We also demonstrate that non-smooth surfaces can play a key role in the energy conversion enhancements obtained through topology optimization. Finally, we examine the relative benefits of flexoelectricity, and surface piezoelectricity on the energy conversion efficiency of nanobeams. We find that the energy conversion efficiency of flexoelectric nanobeams is comparable to the energy conversion efficiency obtained from nanobeams whose electromechanical coupling occurs through surface piezoelectricity, but are ten times thinner. Overall, our results not only demonstrate the utility and efficiency of flexoelectricity as a nanoscale energy conversion mechanism, but also its relative superiority as compared to piezoelectric or surface piezoelectric effects.

© 2017 Elsevier Ltd. All rights reserved.

## 1. Introduction

Piezoelectricity is perhaps the best-known and most widely studied electromechanical energy conversion mechanism (Anton and Sodano, 2007; Roundy, 2005). In particular, piezoelectric energy harvesters have been used to convert ambient mechanical energy into electrical energy (Priya and Inman, 2009; Priya, 2007). Piezoelectricity is defined mathematically through a linear dependence between the electric polarization  $\mathbf{P}$  and the mechanical strain  $\epsilon$  given by

$$P_i = p_{ijk}\epsilon_{jk} \quad (1)$$

where  $\mathbf{p}$  is the third order piezoelectric tensor. While many materials are piezoelectric, many more are not. This is because the piezoelectric effect only exists in materials with non-centrosymmetric crystal structures.

Another electromechanical energy conversion mechanism that has gained attention in recent years is flexoelectricity, which was first noticed in the 1960s (Kogan, 1964; Meyer, 1969). It has historically been less studied than piezoelectricity,

\* Corresponding authors.

E-mail addresses: [nanthakumar@ikm.uni-hannover.de](mailto:nanthakumar@ikm.uni-hannover.de) (S.S. Nanthakumar), [zhuang@ikm.uni-hannover.de](mailto:zhuang@ikm.uni-hannover.de) (X. Zhuang), [parkhs@bu.edu](mailto:parkhs@bu.edu) (H.S. Park), [timon.rabczuk@uni-weimar.de](mailto:timon.rabczuk@uni-weimar.de) (T. Rabczuk).

its better-known electromechanical energy conversion counterpart (Tagantsev, 1986), but has begun to attract significant interest within about the past decade.

The main reason for this is that while in piezoelectricity the polarization is linearly related to the strain, in flexoelectricity the polarization is related to not only the strain, but also the *gradient* of strain (Tagantsev, 1986). When flexoelectric effects are accounted for, the polarization is written as

$$P_i = p_{ijk}\epsilon_{jk} + \mu_{ijkl} \frac{\partial \epsilon_{jk}}{\partial x_l} \quad (2)$$

where  $\mu_{ijkl}$  are the flexoelectric coefficients.

Because flexoelectricity depends upon the gradient of strain, flexoelectricity can, in principle, occur in any dielectric material. This implies that flexoelectricity, and thus energy conversion and harvesting, may be possible from a range of materials where piezoelectricity is not operant. For example, biological membranes, which have no crystalline symmetry to enable piezoelectricity, can exhibit flexoelectricity, particularly when bent, or highly curved (Ahmadpoor and Sharma, 2015; Deng et al., 2014c; Liu and Sharma, 2013; Mohammadi et al., 2014; Petrov, 2001; Todorov et al., 1994). Flexoelectricity can also exploit dimensionality. This is most obvious in nanomaterials, where large strain gradients can more readily be produced (Deng et al., 2014a; Duerloo and Reed, 2013; Dumitrica et al., 2002; Kalinin and Meunier, 2008; Krichen and Sharma, 2016; Majdoub et al., 2008b; Nguyen et al., 2013). Flexoelectricity may also be important for soft materials, where because strain gradients scale inversely with elastic stiffness, the flexoelectric constants may be more than 20 times those of stiff ferroelectrics like barium titanate (Deng et al., 2014c). Furthermore, flexoelectricity may be used to create novel multifunctional materials like apparently piezoelectric composites without using piezoelectric materials, as recently proposed by Sharma and co-workers (Sharma et al., 2010; 2007). Flexoelectricity may be operant at all temperatures, which may be useful in place of piezoelectrics like Barium and Lead Titanate that are piezoelectric only below the Curie temperature (Mbarki et al., 2014). In addition, some of these new material classes may exhibit significantly enhanced piezoelectric strength as compared to well-known piezoelectric materials like barium titanate (BTO) (Catalan et al., 2004; Cross, 2006; Jiang et al., 2013; Krichen and Sharma, 2016; Nguyen et al., 2013; Yudin and Tagantsev, 2013; Zubko et al., 2013). Finally, we note other recent experimental (Baskaran et al., 2011; Bhaskar et al., 2015; Catalan et al., 2011; Chu et al., 2009; Huang et al., 2011; Lu et al., 2012; Ma and Cross, 2003; 2006; Zhu et al., 2006), theoretical (Abdollahi et al., 2014a; Liu et al., 2012; Mao and Purohit, 2015; Maranganti et al., 2006; Shen and Hu, 2010; Stengel, 2013; Yan and Jiang, 2013; Yang et al., 2015) and a few computational (Abdollahi et al., 2015a; 2014a; 2015b) investigations of flexoelectric phenomena in various materials, structures, and configurations.

A key issue that has not been addressed to-date is how the principles underlying flexoelectricity can be fully exploited to design advanced engineering structures with enhanced piezoelectric strength and electromechanical coupling. First, the computational complexity of discretizing and solving the fourth order partial differential equations of flexoelectricity has resulted in very few computational finite element (FE) methods (Abdollahi et al., 2015a; 2014a; 2015b; Mao et al., 2016; Yvonne and Liu, 2017). Furthermore, while FE-based topology optimization approaches, which have emerged within the past 15 years as the computational design tool of choice for many complex engineering problems (Bendsoe and Kikuchi, 1988; Deaton and Grandhi, 2014; Rozvany, 2001; Sigmund and Maute, 2013), do exist for piezoelectricity, i.e. Silva and Kikuchi (1999), Rupp et al. (2009), Zheng et al. (2009b), Chen et al. (2010) and Nanthakumar et al. (2016), few if any such approaches have been developed for flexoelectricity, i.e. the isogeometric approach for flexoelectric structures as recently proposed by Ghasemi et al. (2017).

In the present work, we develop a computational model to perform topology optimization of flexoelectric structures in order to maximize their intrinsic material performance with regards to the energy conversion potential of flexoelectric nanostructures. The higher order equations of flexoelectricity are discretized using a mixed finite element formulation similar to that proposed in Shu et al. (1999). The topology optimization is performed adopting the level set based optimization scheme proposed by Allaire et al. (2004). After deriving the optimization framework, we use it to examine the enhancements in energy conversion efficiency that is possible in flexoelectric Barium Titanate (BTO) nanobeams using optimization. We emphasize that the focus of this paper is not on the flexoelectric performance of BTO. Instead, we choose BTO as a matter of convenience because it is flexoelectric, and because it is electromechanically well-characterized, in terms of knowledge of the surface piezoelectric (Dai et al., 2011) and bulk flexoelectric properties (Berlincourt and Jaffe, 1958).

We focus our discussion into two segments. First, we demonstrate the significant enhancements in energy conversion efficiency that can be obtained by performing topology optimization of flexoelectric nanobeams. Second, we compare the energy conversion benefits of flexoelectricity compared to piezoelectricity and surface piezoelectricity in nanobeams. In doing so, we find that significantly smaller piezoelectric nanobeams are needed to match the energy conversion efficiency obtained using larger flexoelectric nanobeams.

## 2. Flexoelectricity and surface piezoelectricity

The mathematical modeling of flexoelectric behavior is based on the extended linear theory of piezoelectricity with additional strain gradient terms. In Shen and Hu (2010), a general internal energy density function ( $U$ ) involving strain energy, electrostatic energy and their corresponding strain gradients was presented. Within the extended theory of dielectrics, the internal energy density function including flexoelectricity, piezoelectricity, surface elastic and piezoelectric effects can be

written as summation of bulk ( $U_b$ ) and surface ( $U_s$ ) energy as follows,

$$U = U_b + U_s$$

$$U_b = \frac{1}{2} \boldsymbol{\epsilon} : \mathbf{C} : \boldsymbol{\epsilon} - \mathbf{E} \cdot \mathbf{e} : \boldsymbol{\epsilon} - \mathbf{E} \cdot \mathbf{h} : \boldsymbol{\eta} - \frac{1}{2} \mathbf{E} \cdot \boldsymbol{\kappa} \cdot \mathbf{E} + \frac{1}{2} \boldsymbol{\eta} : \mathbf{g} : \boldsymbol{\eta}$$

$$U_s = U_{s0} + \boldsymbol{\alpha}_s : \boldsymbol{\epsilon}_s + \boldsymbol{\omega}_s \cdot \mathbf{E}_s + \frac{1}{2} \boldsymbol{\epsilon}_s : \mathbf{C}_s : \boldsymbol{\epsilon}_s - \mathbf{E}_s \cdot \mathbf{e}_s : \boldsymbol{\epsilon}_s - \frac{1}{2} \mathbf{E}_s \cdot \boldsymbol{\kappa}_s \cdot \mathbf{E}_s \quad (3)$$

where the subscript  $s$  in the above equations denote the surface terms.  $\boldsymbol{\epsilon}$  and  $\boldsymbol{\epsilon}_s$  are the bulk and surface strain tensor and  $\mathbf{E}$  and  $\mathbf{E}_s$  are the bulk and surface electric field vectors,  $\boldsymbol{\eta}$  is the strain gradient tensor,  $\mathbf{C}$  and  $\mathbf{C}_s$  are the fourth order stiffness tensors,  $\mathbf{e}$  and  $\mathbf{e}_s$  are the third order piezoelectric coupling tensors,  $\boldsymbol{\kappa}$  and  $\boldsymbol{\kappa}_s$  are the dielectric permittivity tensors,  $\mathbf{g}$  is the sixth order strain gradient elasticity tensor and  $\mathbf{h}$  is the fourth order flexoelectric tensor which captures both strain-polarization gradient coupling and strain gradient-polarization coupling.

The tensor  $\mathbf{h} = \mathbf{d} - \mathbf{f}$ , where the coupling tensors  $\mathbf{d}$  and  $\mathbf{f}$  correspond to the converse and direct flexoelectric effects, respectively. The bulk physical stress and electric displacement as defined in Sharma et al. (2010), can be obtained from the energy density function as

$$\boldsymbol{\sigma}^b = \boldsymbol{\sigma} - \nabla \cdot \boldsymbol{\tau} = \frac{\partial U_b}{\partial \boldsymbol{\epsilon}} - \nabla \cdot \left( \frac{\partial U_b}{\partial \boldsymbol{\eta}} \right) = \mathbf{C} : \boldsymbol{\epsilon} - \mathbf{E} \cdot \mathbf{e} + \nabla \mathbf{E} : \mathbf{h} \quad (4)$$

$$\mathbf{D}^b = -\mathbf{D} - \nabla \cdot \mathbf{Q} = -\frac{\partial U_b}{\partial \mathbf{E}} - \nabla \cdot \left( \frac{\partial U_b}{\partial \nabla \mathbf{E}} \right) = \mathbf{e} \cdot \boldsymbol{\epsilon} + \boldsymbol{\kappa} \cdot \mathbf{E} + \mathbf{h} : \boldsymbol{\eta} \quad (5)$$

where the electric displacement gradient  $\mathbf{Q}$  in Eq. (5) is zero as there is no electric field gradient in Eq. (3). In Eq. (4), the terms involving the gradient of  $\boldsymbol{\eta}$  are ignored. The surface mechanical stress and electric displacement are,

$$\boldsymbol{\sigma}_s = \boldsymbol{\alpha}_s + \mathbf{C}_s : \boldsymbol{\epsilon}_s - \mathbf{e}_s \cdot \mathbf{E}_s$$

$$\mathbf{D}_s = \boldsymbol{\omega}_s + \mathbf{e}_s^T : \boldsymbol{\epsilon}_s + \boldsymbol{\kappa}_s \cdot \mathbf{E}_s \quad (6)$$

where the terms  $\boldsymbol{\alpha}_s$  and  $\boldsymbol{\omega}_s$  are the residual surface stress and electric displacement respectively.

### 3. Numerical formulation for flexoelectric beam

The fourth order PDEs of flexoelectricity necessitates  $C^1$  continuous basis functions for a Galerkin FE method, which classical Lagrange polynomials cannot satisfy. Though the literature on computational models for flexoelectricity is in its infancy, various approaches have already been proposed to satisfy the  $C^1$  continuity requirement. In Yvonnet and Liu (2017), a linear triangular element is used to discretize the electric potential while a  $C^1$  triangular Argyris element is used to discretize the mechanical displacements. In the current work and in Mao et al. (2016), a mixed FE formulation with  $C^0$  continuous element is used for solving the flexoelectric governing equations. In the works by Abdollahi and co-workers, a meshfree maximum entropy interpolate was used to satisfy the  $C^1$  continuity requirement (Abdollahi et al., 2015a; 2014a; 2015b). We note that the emphasis of this work lies in the application of a numerical method that works for flexoelectricity (demonstrated through the validation example in Section 5.1) to perform topology optimization, and through the topology optimization discern the relative benefits of piezo and flexoelectric contributions to nanoscale energy harvesting. Therefore, our FEM approach is distinct from previous approaches, though we have not performed a conclusive or exhaustive analysis to determine if, and how, it is better, as our major concern was to have a relatively simple FEM model that could easily be extended for topology optimization applications.

Therefore, a mixed FE formulation for analyzing flexoelectric structures is adopted in this work. The  $C^1$  displacement continuity is circumvented by using displacement,  $\mathbf{u}$  and displacement gradients,  $\boldsymbol{\psi}$  as independent unknowns while compatibility between master field  $\boldsymbol{\psi}$  and slave field  $\nabla \mathbf{u}$  obtained from the kinematics relation is enforced in the weak form. The elements require only  $C^0$  continuity. Lagrange multipliers are used to enforce the kinematic constraints between displacements and their gradients. Mixed FE formulations for strain gradient elasticity are proposed in Shu et al. (1999) and Amanatidou and Aravas (2002). The mixed finite element formulation proposed in Amanatidou and Aravas (2002) is extended to accommodate flexoelectricity recently in Mao et al. (2016). A mixed finite element proposed in Shu et al. (1999) is adopted in the present work.

The weak form of mechanical and electrostatic equilibrium is obtained by finding the  $\mathbf{u} \in \{\mathbf{u} = \bar{\mathbf{u}} \text{ on } \Gamma, \mathbf{u} \in H^1(\Omega)\}$ ,  $\boldsymbol{\psi} \in \{\boldsymbol{\psi} = \bar{\boldsymbol{\psi}} \text{ on } \Gamma, \boldsymbol{\psi} \in H^1(\Omega)\}$ ,  $\boldsymbol{\phi} \in \{\boldsymbol{\phi} = \bar{\boldsymbol{\phi}} \text{ on } \Gamma, \boldsymbol{\phi} \in H^1(\Omega)\}$ ,  $\boldsymbol{\lambda} \in L^2(\Omega)$ , similarly  $\delta \mathbf{u} \in \{\delta \mathbf{u} = 0 \text{ on } \Gamma, \delta \mathbf{u} \in H^1(\Omega)\}$ ,  $\delta \boldsymbol{\psi} \in \{\delta \boldsymbol{\psi} = 0 \text{ on } \Gamma, \delta \boldsymbol{\psi} \in H^1(\Omega)\}$ ,  $\delta \boldsymbol{\phi} \in \{\delta \boldsymbol{\phi} = 0 \text{ on } \Gamma, \delta \boldsymbol{\phi} \in H^1(\Omega)\}$  and  $\delta \boldsymbol{\lambda} \in L^2(\Omega)$  such that,

$$\delta \Pi = \int_{\Omega} \left( \boldsymbol{\sigma} : \boldsymbol{\epsilon}(\delta \mathbf{u}) + \hat{\boldsymbol{\tau}} : \hat{\boldsymbol{\eta}}(\delta \boldsymbol{\psi}) - \mathbf{D} \cdot \mathbf{E}(\delta \boldsymbol{\phi}) \right) d\Omega + \int_{\Omega} \boldsymbol{\lambda} : (\delta \boldsymbol{\psi} - \nabla \delta \mathbf{u}) d\Omega$$

$$+ \int_{\Gamma} (\boldsymbol{\sigma}_s : \boldsymbol{\epsilon}_s(\delta \mathbf{u}) - \mathbf{D}_s \cdot \mathbf{E}_s(\delta \boldsymbol{\phi})) d\Gamma + \int_{\Omega} (\boldsymbol{\psi} - \nabla \mathbf{u}) : \delta \boldsymbol{\lambda} d\Omega$$

$$- \int_{\Gamma} \boldsymbol{\epsilon}_s(\delta \mathbf{u}) : \boldsymbol{\alpha}_s d\Gamma - \int_{\Gamma} \mathbf{E}_s(\delta \boldsymbol{\phi}) \cdot \boldsymbol{\omega}_s d\Gamma - \int_{\Gamma_N} \delta \mathbf{u} \cdot \bar{\mathbf{t}} d\Gamma - \int_{\Omega} \delta \mathbf{u} \cdot \mathbf{b} d\Omega = 0 \quad (7)$$

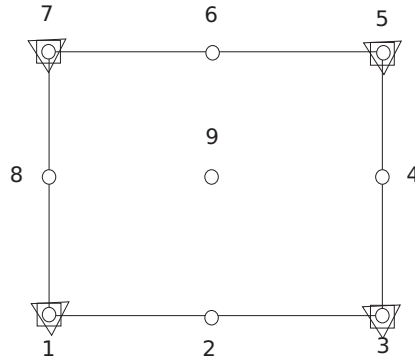


Fig. 1. A nine noded flexoelectric element. DOF at circles -  $u_1, u_2$ , at squares -  $\psi_{11}, \psi_{12}, \psi_{21}, \psi_{22}$  and  $\phi$ , at triangle -  $\lambda_{11}, \lambda_{12}, \lambda_{21}, \lambda_{22}$ .

$$\begin{aligned}
 & \int_{\Omega} \boldsymbol{\epsilon}(\delta \mathbf{u}) : \mathbf{C} : \boldsymbol{\epsilon}(\mathbf{u}) d\Omega - \int_{\Omega} \boldsymbol{\epsilon}(\delta \mathbf{u}) : \mathbf{e} \cdot \mathbf{E}(\phi) d\Omega - \int_{\Omega} \nabla \delta \mathbf{u} : \boldsymbol{\lambda} d\Omega \\
 & + \int_{\Gamma} \boldsymbol{\epsilon}_s(\delta \mathbf{u}) : \mathbf{C}_s : \boldsymbol{\epsilon}_s(\mathbf{u}) d\Gamma - \int_{\Gamma} \boldsymbol{\epsilon}_s(\delta \mathbf{u}) : \mathbf{e}_s \cdot \mathbf{E}_s(\phi) d\Gamma \\
 & - \int_{\Omega} \hat{\boldsymbol{\eta}}(\delta \boldsymbol{\psi}) : \mathbf{h} \cdot \mathbf{E}(\phi) d\Omega + \int_{\Omega} \hat{\boldsymbol{\eta}}(\delta \boldsymbol{\psi}) : \mathbf{g} : \hat{\boldsymbol{\eta}}(\boldsymbol{\psi}) d\Omega + \int_{\Omega} \delta \boldsymbol{\psi} : \boldsymbol{\lambda} d\Omega \\
 & + \int_{\Omega} \mathbf{E}(\delta \phi) \cdot \mathbf{e} : \boldsymbol{\epsilon}(\mathbf{u}) d\Omega + \int_{\Omega} \mathbf{E}(\delta \phi) \cdot \mathbf{h} : \hat{\boldsymbol{\eta}}(\boldsymbol{\psi}) d\Omega + \int_{\Omega} \mathbf{E}(\delta \phi) \cdot \boldsymbol{\kappa} \cdot \mathbf{E}(\phi) d\Omega \\
 & + \int_{\Gamma} \mathbf{E}_s(\delta \phi) \cdot \mathbf{e}_s : \boldsymbol{\epsilon}_s(\mathbf{u}) d\Gamma + \int_{\Gamma} \mathbf{E}_s(\delta \phi) \cdot \boldsymbol{\kappa}_s \cdot \mathbf{E}_s(\phi) d\Gamma \\
 & - \int_{\Omega} \delta \boldsymbol{\lambda} : \nabla \mathbf{u} d\Omega + \int_{\Omega} \delta \boldsymbol{\lambda} : \boldsymbol{\psi} d\Omega \\
 & = \int_{\Gamma} \boldsymbol{\epsilon}_s(\delta \mathbf{u}) : \boldsymbol{\alpha}_s d\Gamma + \int_{\Gamma_N} \delta \mathbf{u} \cdot \bar{\mathbf{t}} d\Gamma + \int_{\Omega} \delta \mathbf{u} \cdot \mathbf{b} d\Omega + \int_{\Gamma} \mathbf{E}_s(\delta \phi) \cdot \boldsymbol{\omega}_s d\Gamma
 \end{aligned} \quad (8)$$

where  $\hat{\boldsymbol{\tau}} = \frac{\partial \mathbf{u}}{\partial \hat{\boldsymbol{\eta}}}$  and  $\hat{\boldsymbol{\eta}}$  is the third order tensor related to relaxed displacement gradient  $\boldsymbol{\psi}$  as  $\hat{\boldsymbol{\eta}} = \frac{1}{2}(\psi_{jk,i} + \psi_{ik,j})$ . The constraint  $\boldsymbol{\psi} = \nabla \mathbf{u}$  is imposed in a weighted residual manner by including  $\delta \int_{\Omega} (\boldsymbol{\psi} - \nabla \mathbf{u}) : \boldsymbol{\lambda} d\Omega$  in Eq. (7). In the case of energy harvesting applications, the structure is subjected to purely mechanical loading, so the electric boundary conditions and loads are not considered in Eq. (7). In Eq. (8),  $\mathbf{g}$  is the sixth order tensor corresponding to strain gradient elasticity, the components of which are as defined in Abdollahi et al. (2015a). In the present work the energy contribution due to strain gradient elasticity is not considered. In order to have a well conditioned stiffness matrix, the terms involving  $\mathbf{g}$  are not completely removed while relatively small values for  $\mathbf{g}$  are assumed.

A nine noded isoparametric element for analyzing flexoelectric 2D structures is developed in this work. The element has displacement degrees of freedom  $u_1, u_2$  at all the nodes, relaxed displacement gradients  $\psi_{11}, \psi_{12}, \psi_{21}$  and  $\psi_{22}$  at the 4 corner nodes and electric potential  $\phi$  at the 4 corner nodes. In addition to these DOFs, the element has four Lagrange multipliers  $\lambda_{11}, \lambda_{12}, \lambda_{21}$  and  $\lambda_{22}$  assumed constant throughout the element.

Shu et al. (1999) presented two different types of quadrilateral nine noded elements based on the number of lagrange multiplier DOFs. They are named QU34L16 and QU34L4. In QU34L16, 4 Lagrange multipliers  $\lambda_{ij}$  are bilinearly interpolated between nodal values given at the four quadrature points of a  $2 \times 2$  Gauss integration scheme, for a total of 16 nodal values of Lagrange multipliers.

In the present work, based on the elements discussed in Shu et al. (1999), a mixed FE element to accommodate the coupled flexoelectric effect is proposed. The flexoelectric element used in the present work along with the degrees of freedom is shown in the Fig. 1. The displacements  $u_1, u_2$  are interpolated using biquadratic shape functions,  $N^q$ . The relaxed displacement gradients,  $\psi_{11}, \psi_{12}, \psi_{21}, \psi_{22}$ , lagrange multipliers,  $\lambda_{11}, \lambda_{12}, \lambda_{21}, \lambda_{22}$  and electric potential,  $\phi$  are interpolated using bilinear shape functions,  $N^l$ . An inf-sup test to prove the stability of the proposed element is shown in Appendix C. The FE approximation is as shown below,

$$\begin{aligned}
 u^h(x) &= \sum_{i=1}^9 \mathbf{N}_i^q \mathbf{u}_i ; \quad \psi^h(x) = \sum_{i=1,3,5,7} \mathbf{N}_i^l \boldsymbol{\psi}_i \\
 \phi^h(x) &= \sum_{i=1,3,5,7} \mathbf{N}_i^l \phi_i ; \quad \lambda^h(x) = \sum_{i=1,3,5,7} \mathbf{N}_i^l \lambda_i
 \end{aligned} \quad (9)$$

$$\begin{aligned}\delta u^h(x) &= \sum_{i=1}^9 \mathbf{N}_i^q \delta \mathbf{u}_i; \quad \delta \psi^h(x) = \sum_{i=1,3,5,7} \mathbf{N}_i^l \delta \psi_i \\ \delta \phi^h(x) &= \sum_{i=1,3,5,7} \mathbf{N}_i^l \delta \phi_i; \quad \delta \lambda^h(x) = \sum_{i=1,3,5,7} \mathbf{N}_i^l \delta \lambda_i\end{aligned}\quad (10)$$

By substituting the above discrete representation in Eq. (8) we obtain the following function in terms of nodal degrees of freedom,

$$\begin{aligned}& \delta \mathbf{u}^T \int_{\Omega} \mathbf{B}_u^T \mathbf{C} \mathbf{B}_u d\Omega \mathbf{u} - \delta \mathbf{u}^T \int_{\Omega} \mathbf{B}_u^T \mathbf{e}^T \mathbf{B}_{\phi} d\Omega \phi - \delta \mathbf{u}^T \int_{\Omega} \mathbf{B}_{\psi u}^T \mathbf{N}_{\lambda} d\Omega \lambda \\ & + \delta \mathbf{u}^T \int_{\Gamma} \mathbf{B}_u^T \mathbf{M}_p^T \mathbf{C}_s \mathbf{M}_p \mathbf{B}_u d\Gamma \mathbf{u} - \delta \mathbf{u}^T \int_{\Gamma} \mathbf{B}_u^T \mathbf{M}_p^T \mathbf{e}_s^T \mathbf{P}_{\phi} \mathbf{B}_{\phi} d\Gamma \phi \\ & - \delta \psi^T \int_{\Omega} \mathbf{H}^T \mathbf{h}^T \mathbf{B}_{\phi} d\Omega \phi + \delta \psi^T \int_{\Omega} \mathbf{H}^T \mathbf{g} \mathbf{H} d\Omega \psi + \delta \psi^T \int_{\Omega} \mathbf{N}^T \mathbf{N}_{\lambda} d\Omega \lambda \\ & + \delta \phi^T \int_{\Omega} \mathbf{B}_{\phi}^T \mathbf{e} \mathbf{B}_u d\Omega \mathbf{u} + \delta \phi^T \int_{\Omega} \mathbf{B}_{\phi}^T \mathbf{h} \mathbf{H} d\Omega \psi + \delta \phi^T \int_{\Omega} \mathbf{B}_{\phi} \kappa \mathbf{B}_{\phi} d\Omega \phi \\ & + \delta \phi^T \int_{\Gamma} \mathbf{B}_{\phi}^T \mathbf{P}_{\phi}^T \mathbf{e}_s \mathbf{M}_p \mathbf{B}_u d\Gamma \mathbf{u} + \delta \phi^T \int_{\Gamma} \mathbf{B}_{\phi}^T \mathbf{P}_{\phi}^T \kappa_s \mathbf{P}_{\phi} \mathbf{B}_{\phi} d\Gamma \phi \\ & - \delta \lambda^T \int_{\Omega} \mathbf{N}_{\lambda} \mathbf{B}_{\psi u} d\Omega \mathbf{u} + \delta \lambda^T \int_{\Omega} \mathbf{N}_{\lambda} \mathbf{N}^l d\Omega \psi \\ & = \delta \mathbf{u}^T \int_{\Gamma_N} \mathbf{N}^q \mathbf{t} d\Gamma + \delta \mathbf{u}^T \int_{\Omega} \mathbf{N}^q \mathbf{b} d\Omega\end{aligned}\quad (11)$$

$$\text{where, } \mathbf{B}_u = \begin{bmatrix} \frac{\partial N^q}{\partial x} & 0 \\ 0 & \frac{\partial N^q}{\partial y} \\ \frac{\partial N^q}{\partial y} & \frac{\partial N^q}{\partial x} \end{bmatrix}, \quad \mathbf{B}_{\phi} = \begin{bmatrix} \frac{\partial N^l}{\partial x} \\ \frac{\partial N^l}{\partial y} \end{bmatrix}, \quad \mathbf{H} = \begin{bmatrix} \frac{\partial N^l}{\partial x} & 0 & 0 & 0 \\ 0 & \frac{\partial N^l}{\partial y} & 0 & 0 \\ 0 & \frac{\partial N^l}{\partial x} & \frac{\partial N^l}{\partial x} & 0 \\ \frac{\partial N^l}{\partial y} & 0 & 0 & 0 \\ 0 & 0 & 0 & \frac{\partial N^l}{\partial y} \\ 0 & 0 & \frac{\partial N^l}{\partial y} & \frac{\partial N^l}{\partial y} \end{bmatrix}, \quad \mathbf{B}_{\psi u} = \begin{bmatrix} \frac{\partial N^l}{\partial x} & 0 \\ 0 & \frac{\partial N^l}{\partial x} \\ \frac{\partial N^l}{\partial y} & 0 \\ 0 & \frac{\partial N^l}{\partial y} \end{bmatrix}, \quad \mathbf{N}_{\lambda} = \mathbf{I}_{4 \times 4}.$$

$$\mathbf{M}_p = \begin{pmatrix} P_{11}^2 & P_{12}^2 & P_{11}P_{12} \\ P_{12}^2 & P_{22}^2 & P_{12}P_{22} \\ 2P_{11}P_{12} & 2P_{12}P_{22} & P_{12}^2 + P_{11}P_{22} \end{pmatrix}\quad (12)$$

where  $\mathbf{P} = \mathbf{I} - \mathbf{n} \otimes \mathbf{n}$  and  $\mathbf{P}_{\phi} = \mathbf{n} \otimes \mathbf{n}$  are the tangential and normal projection tensors, respectively, which enables capturing the tangential and normal polarization induced by surface piezoelectricity (Nanthakumar et al., 2016; Shen and Hu, 2010). The algebraic equations to be solved to obtain displacement and electric potential in a flexoelectric structure are,

$$\begin{bmatrix} \mathbf{K}_{uu} + \mathbf{K}_{uu}^s & 0 & \mathbf{K}_{u\phi} + \mathbf{K}_{u\phi}^s & \mathbf{K}_{u\lambda} \\ 0 & \mathbf{K}_{\psi\psi} & \mathbf{K}_{\psi\phi} & \mathbf{K}_{\psi\lambda} \\ \mathbf{K}_{\phi u} + \mathbf{K}_{\phi u}^s & \mathbf{K}_{\phi\psi} & -(\mathbf{K}_{\phi\phi} + \mathbf{K}_{\phi\phi}^s) & 0 \\ \mathbf{K}_{\lambda u} & \mathbf{K}_{\lambda\psi} & 0 & 0 \end{bmatrix} \begin{bmatrix} \mathbf{u} \\ \psi \\ \phi \\ \lambda \end{bmatrix} = \begin{bmatrix} \mathbf{F}_u \\ 0 \\ 0 \\ 0 \end{bmatrix}$$

$$\mathbf{K}_{uu} = \int_{\Omega} \mathbf{B}_u^T \mathbf{C} \mathbf{B}_u d\Omega; \quad \mathbf{K}_{uu}^s = \int_{\Gamma} \mathbf{B}_u^T \mathbf{M}_p^T \mathbf{C}_s \mathbf{M}_p \mathbf{B}_u d\Gamma$$

$$\mathbf{K}_{u\phi} = \int_{\Omega} \mathbf{B}_u^T \mathbf{e}^T \mathbf{B}_{\phi} d\Omega = \mathbf{K}_{\phi u}^T; \quad \mathbf{K}_{u\phi}^s = \int_{\Gamma} \mathbf{B}_u^T \mathbf{M}_p^T \mathbf{e}_s^T \mathbf{P}_{\phi} \mathbf{B}_{\phi} d\Gamma = \mathbf{K}_{\phi u}^{sT}$$

$$\mathbf{K}_{u\lambda} = - \int_{\Omega} \mathbf{B}_{\psi u}^T \mathbf{N}_{\lambda} d\Omega = \mathbf{K}_{\lambda u}^T$$

$$\mathbf{K}_{\psi\phi} = \int_{\Omega} \mathbf{H}^T \mathbf{h} \mathbf{B}_{\phi} d\Omega = \mathbf{K}_{\phi\psi}^T$$

$$\mathbf{K}_{\psi\psi} = \int_{\Omega} \mathbf{B}_{\psi}^T \mathbf{g} \mathbf{B}_{\psi} d\Omega$$

$$\begin{aligned}
\mathbf{K}_{\psi\lambda} &= \int_{\Omega} \mathbf{N}^T \mathbf{N}_{\lambda} d\Omega = \mathbf{K}_{\lambda\psi}^T \\
\mathbf{K}_{\phi\phi} &= \int_{\Omega} \mathbf{B}_{\phi}^T \boldsymbol{\kappa} \mathbf{B}_{\phi} d\Omega ; \quad \mathbf{K}_{\phi\phi}^s = \int_{\Gamma} \mathbf{B}_{\phi}^T \mathbf{P}_{\phi}^T \boldsymbol{\kappa}_s \mathbf{P}_{\phi} \mathbf{B}_{\phi} d\Gamma \\
\mathbf{F}_u &= \int_{\Gamma} \mathbf{N}^q \bar{\mathbf{t}} d\Gamma + \int_{\Omega} \mathbf{N}^q \mathbf{b} d\Omega
\end{aligned} \tag{13}$$

The voids are modeled by an “ersatz material” approach (Li et al., 2012; Nanthakumar et al., 2016), in which the voids are modeled as a weak material, which helps the algorithm to recover from intermediate topologies in which the void boundary intersects the force boundaries. Numerical integration over sub triangles on either side of the interface is done to obtain the stiffness matrices. Note that enrichment functions are not used, and so there is no change in the number of degrees of freedom during the optimization process.

In this work, analysis of pure flexoelectric beams and also beams with flexoelectric and surface piezoelectric effects are performed. The general mixed FE formulation derived is accordingly modified to include the phenomenon of interest.

#### 4. Topology optimization of flexoelectric structures

Optimization of beams with flexoelectric, piezoelectric and surface piezoelectric effects is performed in this work to maximize the energy conversion factor (ECF)  $k$ , which is defined under pure mechanical loading as (Majdoub et al., 2008a; Zheng et al., 2009a),

$$k^2 = \frac{\Pi_e}{\Pi_m} \tag{14}$$

$$\Pi_e = \frac{1}{2} \int_{\Omega} \mathbf{E}(\boldsymbol{\phi})^T \boldsymbol{\kappa} \mathbf{E}(\boldsymbol{\phi}) d\Omega + \frac{1}{2} \int_{\Gamma} \mathbf{E}^s(\boldsymbol{\phi})^T \boldsymbol{\kappa}^s \mathbf{E}^s(\boldsymbol{\phi}) d\Gamma = \frac{1}{2} \boldsymbol{\phi}^T (\mathbf{K}_{\phi\phi} + \mathbf{K}_{\phi\phi}^s) \boldsymbol{\phi} \tag{15}$$

$$\Pi_m = \frac{1}{2} \int_{\Omega} \boldsymbol{\epsilon}(\mathbf{u})^T \mathbf{C} \boldsymbol{\epsilon}(\mathbf{u}) d\Omega + \frac{1}{2} \int_{\Gamma} \boldsymbol{\epsilon}^s(\mathbf{u})^T \mathbf{C}^s \boldsymbol{\epsilon}^s(\mathbf{u}) d\Gamma = \frac{1}{2} \mathbf{u}^T (\mathbf{K}_{uu} + \mathbf{K}_{uu}^s) \mathbf{u} \tag{16}$$

In this work, we account for the effects of bulk elasticity, bulk flexoelectricity, and bulk and surface piezoelectricity on the energy conversion factor. We neglect the effects of strain gradient elasticity, surface flexoelectricity, surface elasticity and permittivity, primarily due to the unavailability of those constants for BTO. Therefore, in the Eqs. (15) and (16),  $\mathbf{C}^s = \mathbf{0}$  and  $\boldsymbol{\kappa}^s = \mathbf{0}$ .

The objective function can be written as a minimization problem as,

$$\text{Minimize } J(\Psi) = \frac{1}{k^2} = \frac{\Pi_m}{\Pi_e} \tag{17}$$

$$\text{Subject to } \int_{\Omega} d\Omega - \bar{V} = 0 \tag{18}$$

$$\text{and } \delta\Pi = 0$$

where Eq. (18) is the (user-defined) volume constraint. The geometry of the flexoelectric domain is defined by the level set function. The optimization problem is solved iteratively and the trial topology is obtained based on the level set function  $\Psi$  in each iteration by solving Hamilton-Jacobi equation

$$\frac{\partial \Psi}{\partial t} + V_n |\nabla \Psi| = 0 \tag{19}$$

The level set function is parameterized using a C2 continuous compactly supported radial basis function (CSRBF) designed by Wendland (1995), as defined in Eq. (20).

$$f(r(x, y)) = \max\{0, (1 - r)^3\} (4r + 1) \tag{20}$$

where  $r$  is the radius of support in a 2D Euclidean space. Similar to the material derivative approach adopted in Nanthakumar et al. (2016), the velocity function  $V_n$  required to update the level set function can be obtained as

$$\begin{aligned}
\mathbf{V}_n &= - \int_{\Omega} 2C_1 \boldsymbol{\epsilon}(\mathbf{u}')^T : \mathbf{C} : \boldsymbol{\epsilon}(\mathbf{u}) d\Omega - \int_{\Omega} 2C_2 \mathbf{E}(\boldsymbol{\phi}')^T : \boldsymbol{\kappa} : \mathbf{E}(\boldsymbol{\phi}) d\Omega \\
&+ \int_{\Omega} \boldsymbol{\epsilon}(\mathbf{u})^T : \mathbf{C} : \boldsymbol{\epsilon}(\mathbf{w}) d\Omega - \int_{\Omega} \boldsymbol{\epsilon}(\mathbf{u})^T : \mathbf{e}^T \cdot \mathbf{E}(\mathbf{v}) d\Gamma - \int_{\Omega} \nabla \mathbf{u} : \boldsymbol{\lambda} d\Omega \\
&- \int_{\Omega} \hat{\boldsymbol{\eta}}(\boldsymbol{\psi})^T : \mathbf{h}^T \cdot \mathbf{E}(\boldsymbol{\gamma}) d\Omega + \int_{\Omega} \boldsymbol{\psi} : \boldsymbol{\lambda} d\Omega
\end{aligned}$$

**Table 1**  
Electromechanical properties of Barium Titanate.

Elastic Constants (Berlincourt and Jaffe, 1958)	Piezoelectric constants (Berlincourt and Jaffe, 1958)	Dielectric constants (Berlincourt and Jaffe, 1958)	Flexoelectric constants (Maranganti and Sharma, 2009)
$C_{11}=275$ GPa	$e_{31}=-2.7$ C/m <sup>2</sup>	$\kappa_{11}=12.5$ nC/Vm	$h_{11}=0.15$ nC/m
$C_{12}=179$ GPa	$e_{33}=3.65$ C/m <sup>2</sup>	$\kappa_{33}=14.4$ nC/Vm	$h_{12}=100$ nC/m
$C_{13}=152$ GPa	$e_{15}=21.3$ C/m <sup>2</sup>		$h_{44}=-1.9$ nC/m
$C_{33}=165$ GPa			
$C_{44}=54$ GPa			

$$\begin{aligned}
 & + \int_{\Omega} \mathbf{E}(\boldsymbol{\phi})^T \cdot \mathbf{e} : \boldsymbol{\epsilon}(\mathbf{w})d\Gamma + \int_{\Omega} \mathbf{E}(\boldsymbol{\phi})^T : \mathbf{h} : \hat{\boldsymbol{\eta}}(\mathbf{v})d\Omega - \int_{\Omega} \mathbf{E}(\boldsymbol{\phi})^T \cdot \boldsymbol{\kappa} \cdot \mathbf{E}(\boldsymbol{\gamma})d\Omega \\
 & + \int_{\Gamma} \mathbf{e}_s(\mathbf{u})^T : \mathbf{e}_s^T \cdot \mathbf{E}_s(\mathbf{v}) \cdot kd\Gamma + \int_{\Gamma} \mathbf{E}_s(\boldsymbol{\phi})^T \cdot \mathbf{e}_s : \boldsymbol{\epsilon}_s(\mathbf{w})kd\Gamma \\
 & + \int_{\Omega} \boldsymbol{\lambda} \cdot \mathbf{v}d\Omega + \int_{\Omega} \boldsymbol{\lambda} \cdot \nabla \mathbf{w}d\Omega
 \end{aligned} \tag{21}$$

where

$$C_1 = \frac{1}{\Pi_e(\boldsymbol{\phi}, \boldsymbol{\phi})} \tag{22}$$

$$C_2 = -\frac{\Pi_m(\mathbf{u}, \mathbf{u})}{\Pi_e(\boldsymbol{\phi}, \boldsymbol{\phi})^2} \tag{23}$$

In Eq. (21),  $\mathbf{u}$ ,  $\boldsymbol{\psi}$  and  $\boldsymbol{\phi}$  are the actual variables while  $\mathbf{w}$ ,  $\mathbf{v}$  and  $\boldsymbol{\gamma}$  are adjoint variables obtained by solving the following adjoint problem,

$$\mathbf{K}_{uu}\mathbf{w} + (\mathbf{K}_{u\boldsymbol{\phi}} + \mathbf{K}_{u\boldsymbol{\phi}}^s)\mathbf{v} + \mathbf{K}_{u\boldsymbol{\lambda}}\boldsymbol{\lambda}_0 = 2C_1\mathbf{K}_{uu}\mathbf{u} \tag{24}$$

$$\mathbf{K}_{\boldsymbol{\psi}\boldsymbol{\phi}}\boldsymbol{\gamma} + \mathbf{K}_{\boldsymbol{\psi}\boldsymbol{\psi}}\mathbf{v} + \mathbf{K}_{\boldsymbol{\psi}\boldsymbol{\lambda}}\boldsymbol{\lambda}_0 = 0 \tag{25}$$

$$(\mathbf{K}_{\boldsymbol{\phi}u} + \mathbf{K}_{\boldsymbol{\phi}u}^s)\mathbf{w} + \mathbf{K}_{\boldsymbol{\phi}\boldsymbol{\psi}}\mathbf{v} + \mathbf{K}_{\boldsymbol{\phi}\boldsymbol{\phi}}\boldsymbol{\gamma} = 2C_2\mathbf{K}_{\boldsymbol{\phi}\boldsymbol{\phi}}\boldsymbol{\phi} \tag{26}$$

$$\mathbf{K}_{u\boldsymbol{\lambda}}\boldsymbol{\lambda}_0 + \mathbf{K}_{\boldsymbol{\psi}\boldsymbol{\lambda}}\boldsymbol{\lambda}_0 = 0 \tag{27}$$

The details of the adjoint equations above can be found in Appendix A.

### 5. Numerical examples

In this section we study the influence of flexoelectricity on the energy harvesting capability of various structures. We also performed topology optimization of these flexoelectric structures to elucidate the potential benefits of optimally designing these structures. In all examples, Barium Titanate (BTO) is the material of choice. Again, the choice of BTO is largely a matter of modeling convenience, because the surface piezoelectric (Dai et al., 2011) and bulk flexoelectric constants are known (Berlincourt and Jaffe, 1958). The elastic, dielectric and piezoelectric properties for tetragonal BTO were taken from Berlincourt and Jaffe (1958), and are shown in Table 1. In the examples, the value of tensor  $\mathbf{g}$  is taken as three orders of magnitude less compared to other material properties in order to neglect the effects of strain gradient elasticity while still getting an acceptable condition number for the stiffness matrix.

#### 5.1. Validation of mixed finite element model

In this section we validate the mixed FE formulation presented in the work. The analytical solution for the ECF for a flexoelectric beam is presented for a 1-D model in Majdoub et al. (2008b) as,

$$k = \frac{\chi}{1 + \chi} \sqrt{\frac{\kappa}{Y} \left( e^2 + 12 \left( \frac{h}{t} \right)^2 \right)} \tag{28}$$

In order to validate our FEM implementation, we assume the following material values :  $Y = 100$  GPa,  $\nu = 0$ ,  $h_{11} = 0$ ,  $h_{12} = 10$  nC/m,  $\kappa_{11} = 0$ ,  $\kappa_{33} = 1$  nC/Vm and  $\chi = 1408$ . The aspect ratio of the beam is maintained as 20 while the depth of beam,  $t$  is varied from 50 to 10 nm. The beam is discretized by  $100 \times 20$  mixed finite elements shown in Fig. 1. The comparison in Fig. 2 shows good agreement between the analytic and FEM solutions. A convergence plot showing the variation of error in ECF with mesh size is as shown in Fig. 3. The mesh size is decreased from  $40 \times 4$  to  $200 \times 10$ .

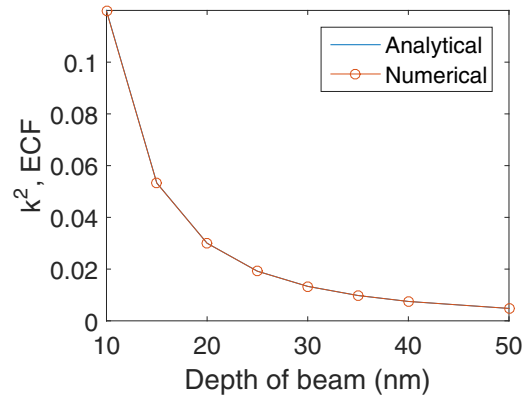


Fig. 2. Comparison between ECF obtained analytically and using the presented mixed FE formulation for a flexoelectric beam.

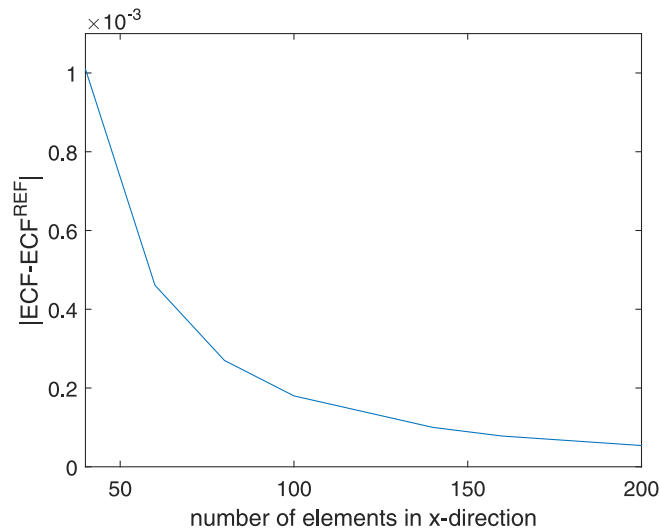


Fig. 3. The variation of error in ECF with mesh size.

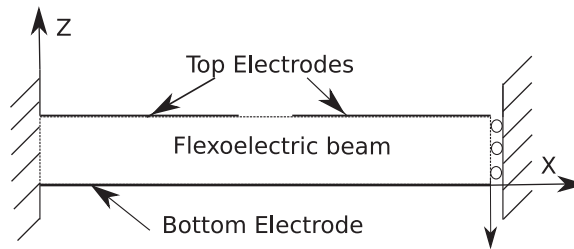


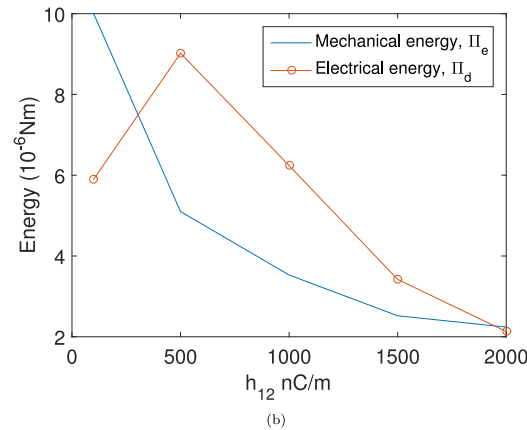
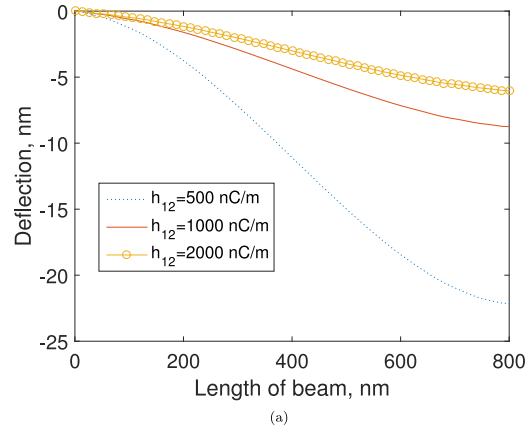
Fig. 4. Schematic showing electrical and mechanical boundary conditions of a flexoelectric beam.

5.2. Flexoelectric nanobeam

Our first example considers a flexoelectric beam similar to the flexural mode composite with BTO plates and Tungsten wires proposed by [Chu et al. \(2009\)](#). The cross section of the plate between the tungsten wires undergoes deformation similar to a beam with fixed ends. As shown in [Fig. 4](#), the beam is fixed at its left end, and while the right end is free to move vertically, its horizontal deflection is constrained. Two electrodes are placed at the top face due to opposite curvatures at either ends of the beam. The bottom electrode is grounded and the top electrodes are free to take any potential value. The beam is subjected to point load of 100 nN at the right end acting vertically downwards (negative Z direction). We consider a nanobeam of this geometry with length 800 nm and height 100 nm.

**Table 2**Relationship between transverse flexoelectric coefficient  $h_{12}$  and energy conversion for a fixed/free beam.

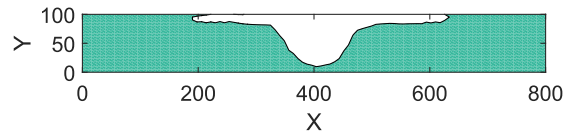
$h_{12}$ (nC/m)	Natural frequency	ECF (Solid)	ECF (Optimal)
50	0.83	0.045	0.18
100	0.91	0.1	0.4
1000	2.58	1.25	1.75
2000	3.83	0.863	1.3
3000	4.2	0.45	0.65

**Fig. 5.** (a) Neutral axis deflection profile of fixed/free beam for different  $h_{12}$  (b) Variation of mechanical and electrical energy with  $h_{12}$ .

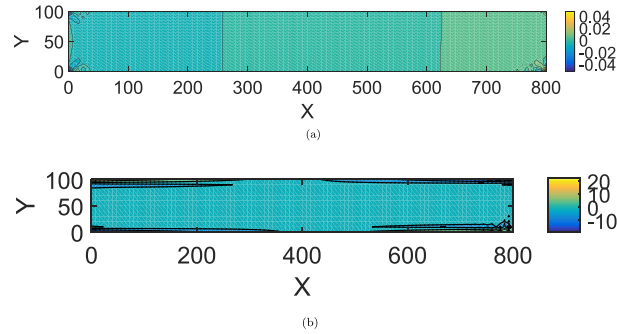
The flexoelectric coefficient  $h_{12}$  of BTO, i.e. the transverse coefficient which plays the major role in flexural motion, is found to differ significantly when determined using *ab initio* methods and when determined experimentally. In Maranganti and Sharma (2009), the value determined by *ab initio* techniques is 5 nC/m, while the one obtained experimentally is on the order of  $10^4$  nC/m (Ma and Cross, 2006). While this inconsistency between experiments and modeling is unfortunate, it does on the other hand present an opportunity to investigate whether simply increasing the flexoelectric coefficients results in an increase of the ECF of fixed/free nano beams.

Table 2 gives the variation of the ECF with varying  $h_{12}$ . The natural frequencies of the nanobeams, which were obtained by solving Eq. (B.1) given in Appendix B, indicate that the stiffness of the fixed beam increases with increasing  $h_{12}$ . This increase in stiffness of the beam decreases the deflection of the beam and when the flexoelectric coefficient  $h_{12}$  becomes larger than 500 nC/m, the energy conversion of the beam begins to decrease despite the continued increase in  $h_{12}$ .

The mechanism underlying this is shown in Fig. 5. Specifically, Fig. 5(a) shows the neutral axis deflection of the nanobeam with varying  $h_{12}$ , where the deflection decreases with increasing  $h_{12}$ . More interestingly, Fig. 5(b) demonstrates the competition between mechanical energy  $\Pi_m$  and electrical energy  $\Pi_e$  as  $h_{12}$  increases. We find that until  $h_{12} \approx 500$  nC/m, the electrical energy increases, in contrast to the decrease in mechanical energy, which results in an enhanced ECF. However, the increasing stiffness due to increasing  $h_{12}$  becomes more important for  $h_{12} > 500$ , due to the reduction in



**Fig. 6.** An optimal topology for maximizing flexoelectric energy conversion of a fixed/free BTO beam of size  $800 \times 100$  nm, and volume ratio of 0.75.



**Fig. 7.** (a) The y-direction gradient of normal strain in x-direction,  $\frac{\partial \epsilon_{11}}{\partial x_2}$  for  $h_{12}=100$  nC/m. (b) The Lagrange multiplier  $\lambda_{11}$ , such that  $\int_{\Omega} (\psi_{11} - \frac{\partial u_1}{\partial x_1}) \delta \lambda_{11} d\Omega = 0$ .

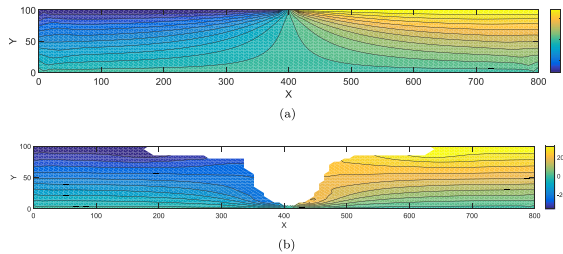


**Fig. 8.** Electric potential distribution across the flexoelectric (a) Solid beam (b) Optimal beam.

the mechanical energy that is available to be converted to electrical energy, which results in a decrease in electrical energy, and thus ECF.

Subsequently we investigate whether optimizing the topology of the beam can improve its energy conversion efficiency. We perform the topology optimization using the formulation presented earlier in this manuscript. The top and bottom surface of the fixed beam, i.e.  $z = 0$  and  $100$  nm respectively, are attached to electrodes as shown in Fig. 4. The electrode at  $z = 0$  nm is grounded to zero potential, whereas the electrode in the top surface of the beam is free. The topology obtained for this beam subject to a volume ratio of 0.76 is shown in Fig. 6. The ECF of the solid beam is 0.045, while the ECF of the optimized beam is 0.17, which demonstrates a 4 times ECF enhancement for the optimum topology. We note that this dramatic increase in ECF was obtained using the value  $h_{12}=100$  nC/m. For values of  $h_{12}$  between 5–100 nC/m, the increase in ECF was always larger than 4 times that of the solid beam, whereas the above this range the increase became smaller than 4 times the solid beam.

This striking increase in the ECF is mainly due to the varying thickness along the length of the beam, which causes an increase in strain gradient due to the decreasing thickness. In Fig. 6, in the region approximately between  $x = 200$  nm and  $x = 600$  nm, the beam height is smaller than the initial height of  $100$  nm due to material removal during the topology optimization. We can understand the removal of the material near the center of the beam through analysis of the gradient of strain  $\epsilon_{xx}$  in the y-direction for the solid beam in Fig. 7. There, the strain gradients are largest closest to the fixed ends of the beam, while the strain gradient is smallest near the beam center. As a result, the materials subject to small strain gradients has been removed in the optimization, leaving the large strain gradient regions to maximize the ECF.

The Lagrange multiplier field,  $\lambda_{11}$  is plotted in Fig. 7(b). The Lagrange multipliers weakly impose the constraint  $\lambda = \nabla \mathbf{u}$ . The Lagrange multiplier changes sign along the x-direction for a constant y-value at the beam mid span, which indicates a change in curvature of the beam. They attain maximum values closer to the constrained ends of the beam.

The effect of the optimization can also be understood through analysis of the electric potential values throughout the beam, where the electric potential distribution of the solid and optimal beams are shown in Figs. 8(a) and 8(b) respectively. Specifically, in the optimized beam in Fig. 8(b), the electric potential values along the top surface have increased with respect to the solid beam, with maximum values in the solid beam being around  $\pm 5$  V, whereas maximum values for the optimal

**Table 3**  
Voltage generated by a solid fixed/free nano beam with flexoelectric effects at its resonant frequency for varying resistance values.

Resistance, $R_l$ ( $G\Omega$ )	Voltage (V)	
	Solid beam	Optimal beam
Inf (Open)	12	22
100	9	16
10	1.2	2
1	0.1	0.12
zero (Closed)	0	0

beam reaching  $\pm 20$  V. The increased voltage increases the electrical energy and consequently the proportion of electrical energy in the total stored energy of the ECF.

We note that, while obtaining the optimal topology the level set function is regularized at fixed intervals in order to prevent the appearance of new holes in the interior of the domain. This is performed by solving the following Hamilton Jacobi equation,

$$\frac{\partial \Psi}{\partial t} + \text{sign}(\Psi_0)(\|\nabla \Psi\| - 1) = 0. \tag{29}$$

Solving this equation gives a signed distance function with respect to an initial isoline,  $\Phi_0$  which prevents appearance of holes and sharp features in the interior of the domain. We did this to prevent the occurrence of several optimal local minima which would in turn prevent obtaining a physically meaningful topology.

### 5.3. Ambient vibrations

In this section, we focus on an example corresponding to situations in which flexoelectric beams can extract energy from the environment from ambient vibrations. Within this context, this means to investigate the behavior of flexoelectric beams under harmonic loads, where the boundary conditions for the problem are the same as the previous problem.

The voltage generated under varying resistance values is obtained by solving the following system of equations whose derivation is shown in Appendix B

$$\begin{bmatrix} -\omega^2 \mathbf{M} + j\omega \mathbf{C} + \mathbf{K}_{uu} & 0 & 0 & \mathbf{K}_{u\lambda} \\ 0 & \mathbf{K}_{\psi\psi} & \mathbf{K}_{\psi\phi} & \mathbf{K}_{\psi\lambda} \\ 0 & j\omega \mathbf{K}_{\phi\psi} & \frac{1}{R_l} + j\omega \mathbf{K}_{\phi\phi} & 0 \\ \mathbf{K}_{\lambda u} & \mathbf{K}_{\lambda\psi} & 0 & 0 \end{bmatrix} \begin{bmatrix} \mathbf{u} \\ \psi \\ \phi \\ \lambda \end{bmatrix} = \begin{bmatrix} \mathbf{F}_0 \\ 0 \\ 0 \\ 0 \end{bmatrix} \tag{30}$$

The variable  $R_l$  is the external resistive load connected to the energy harvester. Open and closed circuit boundary conditions can be obtained when  $R_l = \text{Inf}$  and  $R_l = 0$ , respectively. The external  $R_l$  can be adjusted to obtain required magnitude of output voltage and output current. The fundamental frequency of the solid beam is found to be 0.9 rad/s under open circuit. The maximum voltage generated by the solid fixed/free beam for varying resistance values under a point load at free end with resonant forcing frequency of 0.9 rad/s is provided in Table 3. The fundamental frequency of the optimal beam is 0.74 rad/s under open circuit.

The voltage frequency response function of the optimal beam for a resistance of 1  $G\Omega$  and 100  $G\Omega$  is shown in Fig. 9(a) and 9(b) respectively for the same frequency range. As can be seen the peak of the curve shifts to the right at the higher resistance value indicating that there is an increase in natural frequency of the optimal beam as the open circuit condition is approached. Table 3 also shows the maximum absolute voltage obtained at the electrically free top face of the optimal beam under varying resistance values. Though the mechanical load that is applied at the free end is the same for both the solid and optimal topology, a significantly larger voltage is achieved for the optimal topology, which means a higher ECF as compared to the solid beam at the resonant vibrational frequency. It is evident that the optimal topology has led to an increase in potential values at the electrode face by 200%.

In the present work we have considered a simple circuit with pure resistive load. A more practical energy storage circuit with bridge rectifier and capacitive filter will be adopted in future studies.

### 5.4. Size-dependence of normalized flexoelectric ECF

The polarization due to the flexoelectric effect increases with decreasing size because of its dependence on strain gradient. The optimal topology is tested for decreasing dimensions to examine the size effect. The nanobeam aspect ratio is maintained as 8, while the beam heights were chosen to be 10 nm, 25 nm, 50 nm and 100 nm.

The variation of ECF with dimensions for the solid and optimal topologies is shown in Fig. 10. The ECF as expected increases with decreasing dimension for solid and optimal beam. However, the ECF enhancement for both the solid and optimal topologies leads to a size-independent normalized ECF, which remains about 4 for all the nanobeam dimensions

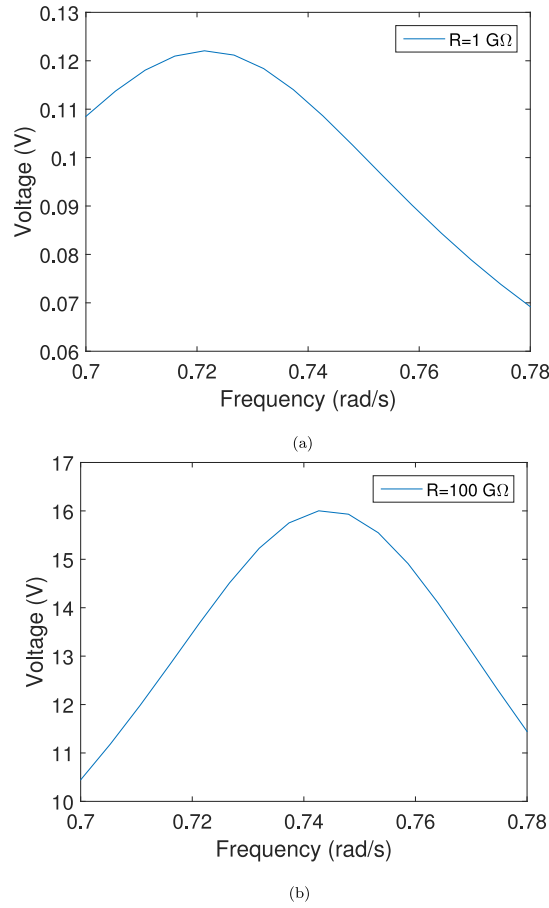


Fig. 9. Voltage frequency response function of optimal beam (a)  $R=1 \text{ G}\Omega$  (b)  $R=100 \text{ G}\Omega$ .

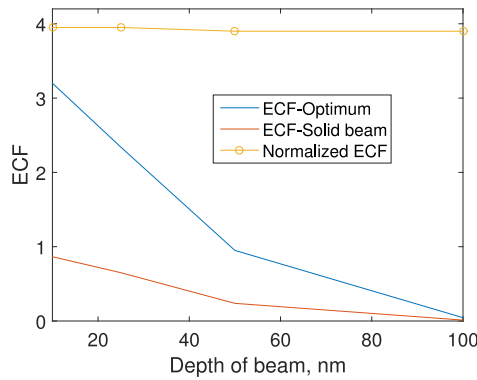


Fig. 10. Variation of ECF of optimal and solid beam with depth of the beam.

ranging from 10 nm to 100 nm. Thus, while larger strain gradients are possible in nanoscale materials, the ECF enhancement that can be gained through topology optimization is unchanged.

### 5.5. Surface piezoelectricity and flexoelectricity

Our last example focuses on investigating the interplay between surface piezoelectricity and flexoelectricity as a function of size for nanobeams with thicknesses smaller than 100 nm. Specifically, we consider two cases. The first is to compare the ECFs for flexoelectric beams and piezoelectric/surface piezoelectric beams, and to determine the length scales at which the energy conversion becomes similar or equivalent. The second is to consider the case when surface piezoelectricity and flexo-

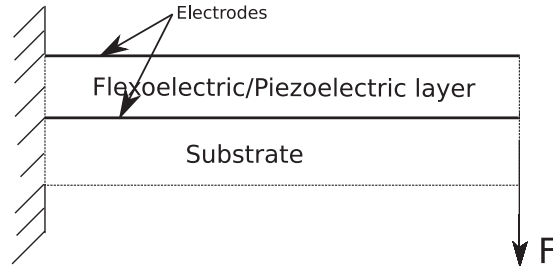


Fig. 11. A cantilever type energy harvester with piezoelectric/flexoelectric layer placed over a substrate.

electricity are considered together, to examine their interplay when the beam dimensions decrease below 100 nm. We note that previous work has considered the effects of piezoelectricity and surface piezoelectricity together (Nanthakumar et al., 2016). We also note that Abdollahi and Arias (2015) recently reported that, for parallel bimorph actuators, flexoelectricity and piezoelectricity exhibit a destructive interplay, thus resulting in a reduction in sensing ability at smaller size scales. The surface piezoelectric effects we consider in this work emerge from the non-centrosymmetry of the surface, and are different from the dramatic enhancements recently observed experimentally by Narvaez et al. (2016) in which the surface piezoelectric response was dramatically enhanced through oxygen doping.

We first examine the relative energy conversion efficiencies that can be gained using either piezoelectricity and surface piezoelectricity, or by using flexoelectricity. To do so, we analyze a cantilever energy harvester with a piezoelectric or flexoelectric layer as shown in Fig. 11 of dimension  $800 \times 100$  nm. The energy harvester is subjected to a point load of 100 nN at the free end. First, the optimization of a tetragonal BTO piezoelectric layer placed over a substrate is performed, in order to examine the possible enhancement in ECF gained through consideration of surface piezoelectricity. The surface piezoelectric constants of BTO is taken from Dai et al. (2011) as  $e_{31}^s = 0.7$  nC/m and  $e_{33}^s = -0.9$  nC/m. The Young's modulus of the substrate material is taken as  $E = 250$  MPa. The piezoelectric layer is optimized for maximum energy conversion with a volume fraction constraint of 0.7. Under open circuit conditions, the ECF of the solid piezoelectric layer without considering surface piezoelectric effects is 0.17. However, when surface piezoelectric effects are considered, the ECF increases only slightly, to 0.19. Thus, the increase in ECF is small even after including surface piezoelectric effects for the  $800 \times 100$  nm BTO nanobeam. We note that we neglect the effects of surface elasticity in this analysis due to the lack of surface elastic constants for BTO.

However, when the nanobeam dimension is reduced to  $80 \times 10$  nm, maintaining the aspect ratio of 8, the ECF of the optimal topology is 0.21. So the inclusion of surface piezoelectricity and optimizing the topology of piezoelectric layer have together lead to an increase of  $\frac{0.21}{0.17} = 1.15$ , i.e. 15% for a  $80 \times 10$  nm beam.

Having examined the enhancements in ECF due to surface piezoelectricity, we now perform optimization of a cubic flexoelectric BTO layer placed over a substrate, as in Fig. 11. The BTO layer has dimensions of  $800 \times 100$  nm, the same as the piezoelectric and surface piezoelectric example above. The substrate is also of the same dimension and with Young's modulus,  $E = 250$  MPa, which is again the same as for the previously discussed piezoelectric/surface piezoelectric example.

Under open circuit condition, the ECF of the solid flexoelectric beam is 0.02. The ECF of the optimal topology is 0.15 leading to an increase in ECF of around eight times compared to solid cantilever flexoelectric layer. Thus, the ECF obtained from an optimal cubic BTO flexoelectric layer of dimension  $800 \times 100$  nm is comparable to an optimal layer of tetragonal BTO with surface piezoelectricity of dimension  $80 \times 10$  nm. This demonstrates that flexoelectricity has a significant influence on the energy conversion efficiency of a cubic, non-piezoelectric material (BTO), an influence that can exceed the energy conversion performance of the equivalent tetragonal piezoelectric BTO. These results also show that for BTO, the increase in ECF using topology optimization is around 8 times for a 100 nm thick nanobeam, whereas the increase in ECF using topology optimization is only about 5% for the same dimension nanobeam considering only piezoelectric and surface piezoelectric effects.

There are also important distinctions in the role the topology optimization plays in enabling energy conversion between piezoelectric and flexoelectric beams. For piezoelectric beams, the ECF is enhanced by redistributing the material, such that strain enhancements in the structure lead to increases in electrical energy due to the piezoelectric coupling.

However, for flexoelectricity, the ECF is enhanced not only by redistribution of material in the nanobeam, but also due to the emergence of stress singularities. Specifically, sharp corners can generate significant local strain gradients, leading to increased local polarization. Fig. 12 shows the optimal topology in (a) and an example topology in (b) for the  $800 \times 100$  nm nanobeam, where the example topology is an artificially created topology that satisfies the same volume constraints as the optimal topology. The example topology was created in order to highlight the effects of the rough surfaces created in Fig. 12(a) in enhancing the ECF. When the removed material results in smooth surfaces as in Fig. 12(b) the ECF is 0.06. In contrast, for the optimal topology with corrugations (Fig. 12(a)) along the surfaces, the ECF is 0.15. The electric potential is higher locally in these locations as shown in Fig. 13 leading to overall increases in electrical energy. This demonstrates the utility of creating non-smooth surfaces within the optimization process as a mechanism to enhancing the flexoelectric energy conversion efficiency.

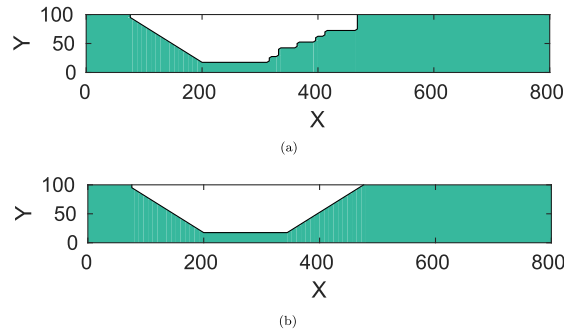


**Fig. 12.** (a) The optimal topology for maximizing energy conversion of a flexoelectric layer in a cantilever energy harvester (volume fraction = 0.7) (b) An example topology with smooth surfaces.

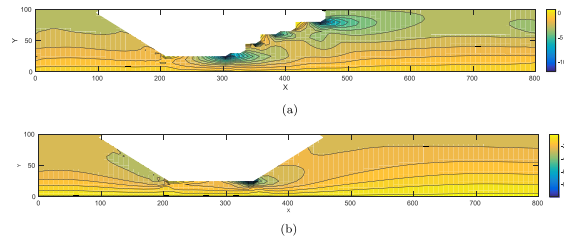


**Fig. 13.** The distribution of electric potential across the cross section of the optimal and example topology in Fig. 12.

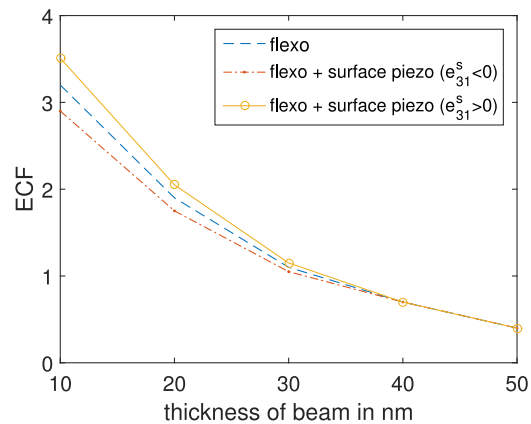


**Fig. 14.** Comparison of variation in optimal ECF with depth of nanobeam of optimal topology made of cubic BTO, for two different cases (a) pure flexoelectric effect (b) flexoelectric and surface piezoelectric effects.

Our last focus within this context is to perform a comparative study to identify the range of BTO nanobeam thicknesses to determine length scales over which flexoelectric or surface piezoelectric effects dominate the energy conversion efficiency, and to examine the interplay between the two effects in contributing to the observed ECF of cubic BTO nanobeams.

To do so, we show in Fig. 14 the variation in optimized ECF for BTO nanobeams with heights smaller than 50 nm. We consider two different cases, one with only flexoelectric effects, and the other with both flexoelectric and surface piezoelectric effects, where the surface piezoelectric coefficients correspond to cubic BTO (Dai et al., 2011). The values of cubic BTO are 6% smaller than the surface coefficients of tetragonal BTO (Dai et al., 2011),  $e_{31}^s = 0.04$  nC/m and  $e_{33}^s = 0.05$  nC/m. The sign of  $e_{31}$  of bulk tetragonal BTO is negative. Also in Hoang et al. (2013), the surface coefficient  $e_{31}^s$  for ZnO is found to be negative. Because of uncertainty on the sign of  $e_{31}^s$  in this example, results are shown for both  $e_{31}^s = 0.04$  nC/m and  $e_{31}^s = -0.04$  nC/m.

As shown in Fig. 14, the surface piezoelectric effect gains significance as the nanobeam depth falls below 30 nm, and positively assists the flexoelectric effect when  $e_{31}^s$  is positive. In contrast, surface piezoelectricity and flexoelectricity interact destructively below 30 nm when  $e_{31}^s$  is negative. In Fig. 14, the ECF due to flexoelectric and surface piezoelectric effects for a nanobeam height of 10 nm is 3.51 for  $e_{31}^s > 0$  while the ECF due to only flexoelectric effect is 3.2. In the total ECF of 3.51 the percentage contribution of flexoelectricity is 91.5% while that of surface piezoelectricity is 8.5%. Overall, Fig. 14 demonstrates that while surface piezoelectricity can either constructively or destructively interact with flexoelectricity to impact the ECF of cubic BTO nanobeams, its effect is relatively small ( $\approx 10\%$ ) even when the nanobeam dimensions shrink to 10 nm or smaller.

## 6. Conclusion

In conclusion, we have presented a mixed finite element formulation that, in conjunction with topology optimization, was used to examine the energy conversion efficiency of nanoscale barium titanate beams. Our simulation have not only demonstrated the increase in energy conversion efficiency that can be gained using topology optimization, but have also demonstrated, for barium titanate, the superiority of flexoelectricity, as compared to piezoelectricity and surface piezoelectricity, as a nanoscale electromechanical energy conversion mechanism.

## Acknowledgment

Authors Xiaoying Zhuang and S.S.Nanthakumar thankfully acknowledge the funding from Sofja Kovalevskaja Award (X. Zhuang in 2015), State Key Laboratory of Structural Analysis for Industrial Equipment (GZ1607). Author Timon Rabczuk acknowledge the financial support by [European Research Council](#) for COMBAT project (Grant number 615132). Harold Park acknowledges the support of the Mechanical Engineering Department at Boston University.

## Appendix A. Derivation of adjoint problem

The objective function and its constraints are as follows,  
Minimize

$$\text{Minimize } J(\Psi) = \frac{1}{k^2} = \frac{\Pi_m}{\Pi_e} \quad (\text{A.1})$$

$$\text{Subject to } \int_{\Omega} d\Omega - \bar{V} = 0 \quad (\text{A.2})$$

$$a(\mathbf{u}, \boldsymbol{\phi}, \boldsymbol{\psi}, \delta\mathbf{u}, \delta\boldsymbol{\phi}, \delta\boldsymbol{\psi}) = l(\delta\mathbf{u}, \delta\boldsymbol{\phi}) \quad (\text{A.3})$$

$$\begin{aligned} \dot{a}(\mathbf{u}, \boldsymbol{\phi}, \boldsymbol{\psi}, \mathbf{w}, \boldsymbol{\gamma}, \mathbf{v}) = & \int_{\Omega} \boldsymbol{\epsilon}^T(\mathbf{u}') : \mathbf{C} : \boldsymbol{\epsilon}(\mathbf{w}) d\Omega + \int_{\Omega} \boldsymbol{\epsilon}^T(\mathbf{u}) : \mathbf{C} : \boldsymbol{\epsilon}(\mathbf{w}') d\Omega + \int_{\Gamma} \boldsymbol{\epsilon}^T(\mathbf{u}) : \mathbf{C} : \boldsymbol{\epsilon}(\mathbf{w}) \cdot \mathbf{V}_n d\Gamma \\ & - \int_{\Omega} \nabla \mathbf{u}' : \boldsymbol{\lambda}_0 d\Omega - \int_{\Omega} \nabla \mathbf{u} : \boldsymbol{\lambda}'_0 d\Omega - \int_{\Gamma} \nabla \mathbf{u} : \boldsymbol{\lambda}_0 \cdot \mathbf{V}_n d\Gamma \\ & - \int_{\Omega} \hat{\boldsymbol{\eta}}(\boldsymbol{\psi}')^T : \mathbf{h}^T \cdot \mathbf{E}(\boldsymbol{\gamma}) d\Omega - \int_{\Omega} \hat{\boldsymbol{\eta}}(\boldsymbol{\psi})^T : \mathbf{h}^T \cdot \mathbf{E}(\boldsymbol{\gamma}') d\Omega - \int_{\Gamma} \hat{\boldsymbol{\eta}}(\boldsymbol{\psi})^T : \mathbf{h}^T \cdot \mathbf{E}(\boldsymbol{\gamma}) \cdot \mathbf{V}_n d\Gamma \\ & + \int_{\Omega} \boldsymbol{\psi}' : \boldsymbol{\lambda}_0 d\Omega + \int_{\Omega} \boldsymbol{\psi} : \boldsymbol{\lambda}'_0 d\Omega + \int_{\Gamma} \boldsymbol{\psi} : \boldsymbol{\lambda}_0 \cdot \mathbf{V}_n d\Gamma \\ & \int_{\Omega} \mathbf{E}(\boldsymbol{\phi})^T \cdot \mathbf{e} : \boldsymbol{\epsilon}(\mathbf{w}') d\Omega - \int_{\Gamma} \mathbf{E}(\boldsymbol{\phi})^T \cdot \mathbf{e} : \boldsymbol{\epsilon}(\mathbf{w}) \cdot \mathbf{V}_n d\Gamma \\ & - \int_{\Omega} \mathbf{E}(\boldsymbol{\phi}')^T \cdot \mathbf{h} : \hat{\boldsymbol{\eta}}(\mathbf{v}) d\Omega - \int_{\Omega} \mathbf{E}(\boldsymbol{\phi})^T \cdot \mathbf{h} : \hat{\boldsymbol{\eta}}(\mathbf{v}') d\Omega - \int_{\Gamma} \mathbf{E}(\boldsymbol{\phi})^T \cdot \mathbf{h} : \hat{\boldsymbol{\eta}}(\mathbf{v}) \cdot \mathbf{V}_n d\Gamma \\ & - \int_{\Omega} \mathbf{E}(\boldsymbol{\phi}')^T \cdot \boldsymbol{\kappa} \cdot \mathbf{E}(\boldsymbol{\gamma}) d\Omega - \int_{\Omega} \mathbf{E}(\boldsymbol{\phi})^T \cdot \boldsymbol{\kappa} \cdot \mathbf{E}(\boldsymbol{\gamma}') d\Omega - \int_{\Gamma} \mathbf{E}(\boldsymbol{\phi})^T \cdot \boldsymbol{\kappa} \cdot \mathbf{E}(\boldsymbol{\gamma}) \cdot \mathbf{V}_n d\Gamma \\ & - \int_{\Gamma} \boldsymbol{\epsilon}_s(\mathbf{u}')^T : \mathbf{e}_s^T \cdot \mathbf{E}_s(\boldsymbol{\psi}) d\Gamma - \int_{\Gamma} \boldsymbol{\epsilon}_s(\mathbf{u})^T : \mathbf{e}_s^T \cdot \mathbf{E}_s(\boldsymbol{\psi}') d\Gamma \\ & - \int_{\Gamma} [\nabla(\boldsymbol{\epsilon}_s(\mathbf{u})^T : \mathbf{e}_s^T \cdot \mathbf{E}_s(\boldsymbol{\psi})) \cdot \mathbf{n} + (\boldsymbol{\epsilon}_s(\mathbf{u})^T : \mathbf{e}_s^T \cdot \mathbf{E}_s(\boldsymbol{\psi})) \eta] \cdot \mathbf{V}_n d\Gamma \\ & - \int_{\Gamma} \mathbf{E}_s(\boldsymbol{\phi}')^T \cdot \mathbf{e}_s : \boldsymbol{\epsilon}_s(\mathbf{w}) d\Gamma - \int_{\Gamma} \mathbf{E}_s(\boldsymbol{\phi})^T \cdot \mathbf{e}_s : \boldsymbol{\epsilon}_s(\mathbf{w}') d\Gamma \\ & - \int_{\Gamma} [\nabla(\mathbf{E}_s(\boldsymbol{\phi})^T \cdot \mathbf{e}_s : \boldsymbol{\epsilon}(\mathbf{w})) \cdot \mathbf{n} + (\mathbf{E}_s(\boldsymbol{\phi})^T \cdot \mathbf{e}_s : \boldsymbol{\epsilon}(\mathbf{w})) \eta] \cdot \mathbf{V}_n d\Gamma \\ & - \int_{\Omega} \boldsymbol{\lambda} : \mathbf{v}' d\Omega + \int_{\Omega} \boldsymbol{\lambda}' : \mathbf{v} d\Omega + \int_{\Gamma} \boldsymbol{\lambda} : \mathbf{v} \cdot \mathbf{V}_n d\Gamma \\ & - \int_{\Omega} \boldsymbol{\lambda} : \nabla \mathbf{w}' d\Omega + \int_{\Omega} \boldsymbol{\lambda}' : \nabla \mathbf{w} d\Omega + \int_{\Gamma} \boldsymbol{\lambda} : \nabla \mathbf{w} \cdot \mathbf{V}_n d\Gamma \end{aligned}$$

$$\dot{l}(\mathbf{w}) = \int_{\Omega} \mathbf{w}' \cdot \mathbf{b} d\Omega + \int_{\Gamma} \mathbf{w} \cdot \mathbf{b} V_n d\Gamma + \int_{\Gamma_N} \mathbf{w}' \cdot \mathbf{t} d\Gamma + \int_{\Gamma_N} (\nabla(\mathbf{w} \cdot \mathbf{t}) \cdot \mathbf{n} + \kappa \mathbf{w} \cdot \mathbf{t}) V_n d\Gamma \quad (\text{A.4})$$

The Lagrangian of the objective functional is,

$$L = J + l(\mathbf{w}) - a(\mathbf{u}, \boldsymbol{\phi}, \boldsymbol{\psi}, \mathbf{w}, \boldsymbol{\gamma}, \mathbf{v}). \quad (\text{A.5})$$

The material derivative of the Lagrangian is defined as ,

$$\dot{L} = \dot{J} + \dot{l}(\mathbf{w}) - \dot{a}(\mathbf{u}, \boldsymbol{\phi}, \boldsymbol{\psi}, \mathbf{w}, \boldsymbol{\gamma}, \mathbf{v}). \quad (\text{A.6})$$

All the terms that contain  $\mathbf{u}'$ ,  $\boldsymbol{\phi}'$  and  $\boldsymbol{\psi}'$  in the material derivative of Lagrangian are collected and the sum of these terms is set to zero, to get the weak form of the adjoint equation,

$$\int_{\Omega} \boldsymbol{\epsilon}^T(\mathbf{u}') : \mathbb{C} : \boldsymbol{\epsilon}(\mathbf{w}) d\Omega - \int_{\Gamma} \boldsymbol{\epsilon}_s(\mathbf{u}')^T : \mathbf{e}_s^T : \mathbf{E}_s(\boldsymbol{\psi}) d\Gamma - \int_{\Omega} \nabla \mathbf{u}' : \boldsymbol{\lambda}_0 d\Omega = \int_{\Omega} 2C_1 \boldsymbol{\epsilon}(\mathbf{u}')^T : \mathbf{C} : \boldsymbol{\epsilon}(\mathbf{u}) d\Omega \quad (\text{A.7})$$

$$- \int_{\Omega} \hat{\boldsymbol{\eta}}(\boldsymbol{\psi}')^T : \mathbf{h}^T : \mathbf{E}(\boldsymbol{\gamma}) d\Omega + \int_{\Omega} \boldsymbol{\psi}' : \boldsymbol{\lambda}_0 d\Omega = 0 \quad (\text{A.8})$$

$$- \int_{\Omega} \mathbf{E}(\boldsymbol{\phi}')^T \cdot \mathbf{h} : \hat{\boldsymbol{\eta}}(\mathbf{v}) d\Omega - \int_{\Omega} \mathbf{E}(\boldsymbol{\phi}')^T \cdot \boldsymbol{\kappa} \cdot \mathbf{E}(\boldsymbol{\psi}) d\Omega - \int_{\Gamma} \mathbf{E}_s(\boldsymbol{\phi}')^T \cdot \mathbf{e}_s : \boldsymbol{\epsilon}_s(\mathbf{w}) d\Gamma = \int_{\Omega} 2C_2 \mathbf{E}(\boldsymbol{\phi}')^T \cdot \boldsymbol{\kappa} \cdot \mathbf{E}(\boldsymbol{\phi}) d\Omega \quad (\text{A.9})$$

## Appendix B. Free vibration and harmonic analysis

Introducing mass and acceleration terms in the Eq. (13) to determine the natural frequency, we have,

$$\begin{bmatrix} \mathbf{M} & 0 & 0 & 0 \\ 0 & 0 & 0 & 0 \\ 0 & 0 & 0 & 0 \\ 0 & 0 & 0 & 0 \end{bmatrix} \begin{bmatrix} \ddot{u} \\ 0 \\ 0 \\ 0 \end{bmatrix} + \begin{bmatrix} \mathbf{K}_{uu} & 0 & 0 & \mathbf{K}_{u\lambda} \\ 0 & \mathbf{K}_{\psi\psi} & \mathbf{K}_{\psi\phi} & \mathbf{K}_{\psi\lambda} \\ 0 & \mathbf{K}_{\phi\psi} & \mathbf{K}_{\phi\phi} & 0 \\ \mathbf{K}_{\lambda u} & \mathbf{K}_{\lambda\psi} & 0 & 0 \end{bmatrix} \begin{bmatrix} \mathbf{u} \\ \boldsymbol{\psi} \\ \boldsymbol{\phi} \\ \boldsymbol{\lambda} \end{bmatrix} = 0 \quad (\text{B.1})$$

The external vibration is assumed harmonic of the form,

$$\mathbf{F} = \mathbf{F}_0 e^{j\omega t} \quad (\text{B.2})$$

The steady state response is also harmonic with the same frequency,

$$\begin{aligned} \mathbf{u}(t) &= \mathbf{u}_0 e^{j\omega t} \\ \boldsymbol{\phi}(t) &= \boldsymbol{\phi}_0 e^{j\omega t} \\ \boldsymbol{\psi}(t) &= \boldsymbol{\psi}_0 e^{j\omega t} \end{aligned} \quad (\text{B.3})$$

By including above equations, the mass and damping matrix, Eq. (30) can be modified as,

$$[-\omega^2 \mathbf{M} + j\omega \mathbf{C} + \mathbf{K}_{uu}] \mathbf{u} + K_l u \boldsymbol{\lambda} = \mathbf{F}_0 \quad (\text{B.4})$$

where  $\mathbf{M} = \int_{\Omega} N^q T \rho N^q d\Omega$  and  $\mathbf{C} = \alpha \mathbf{M} + \beta \mathbf{K}_{uu}$ . The values of  $\alpha$  and  $\beta$  are obtained as described in Deng et al. (2014a).

$$\mathbf{K}_{\psi\psi} \boldsymbol{\psi} + \mathbf{K}_{\psi\phi} \boldsymbol{\phi} + \mathbf{K}_{\psi\lambda} \boldsymbol{\lambda} = 0 \quad (\text{B.5})$$

$$\mathbf{K}_{\phi\psi} \boldsymbol{\psi} + \mathbf{K}_{\phi\phi} \boldsymbol{\phi} + \mathbf{Q} = 0 \quad (\text{B.6})$$

$$\mathbf{K}_{\lambda u} \mathbf{u} + \mathbf{K}_{\lambda\psi} \boldsymbol{\psi} = 0 \quad (\text{B.7})$$

Differentiating Eq. (B.6) with respect to time gives,

$$\mathbf{K}_{\phi\psi} \dot{\boldsymbol{\psi}} + \mathbf{K}_{\phi\phi} \dot{\boldsymbol{\phi}} + \dot{\mathbf{Q}} = 0 \quad (\text{B.8})$$

The energy harvester is connected to a resistor of load  $R_l$ . By considering  $\dot{\mathbf{Q}} = \frac{\phi}{R_l}$  and from Eq. (B.3) we have,

$$j\omega \mathbf{K}_{\phi\psi} \boldsymbol{\psi} + \frac{1}{R_l} + j\omega \mathbf{K}_{\phi\phi} \boldsymbol{\phi} = 0 \quad (\text{B.9})$$

The matrix form of the Eqs. (B.4), (B.5), (B.9), (B.7) is shown in Eq. (30).

## Appendix C. Inf-Sup test

A numerical inf-sup test following the work of Chapelle and Bathe (1993) to examine the mixed FE formulation is performed. The test involves solving an eigenvalue problem, where the minimum eigenvalue is taken as the inf-sup constant,  $\beta$  (Saber et al., 2011). The eigenvalue problem is written as,

$$\mathbf{B}^T \mathbf{M}_{UU}^{-1} \mathbf{B} \mathbf{U} = \beta \mathbf{M}_{\lambda\lambda} \mathbf{U} \quad (\text{C.1})$$

From the algebraic equations derived from the mixed FE formulation of the flexoelectric governing equations, we have,

$$\mathbf{B} = [\mathbf{K}_{\lambda u} \quad \mathbf{K}_{\lambda \psi}]^T \quad (\text{C.2})$$

$\mathbf{M}_{\lambda\lambda}$  is the mass matrix associated to the FE space of Lagrange multiplier field,  $\lambda$ . The plot of inf-sup constant for the flexoelectric element is shown in Fig. C.15. The value shown along the x-axis is the number of elements in the y-direction (elem-y), while the number of elements in the x-direction  $\text{elem-x} = 10 \times \text{elem-y}$ . As stated in Chapelle and Bathe (1993), the element is inf-sup stable if the plot shown in Fig. C.15 is either constant for  $\beta$ , or converges to constant  $\beta$  as the mesh density is increased. The value of  $\log(\beta)$  in Fig. C.15 remains constant and therefore the inf-sup condition is satisfied.

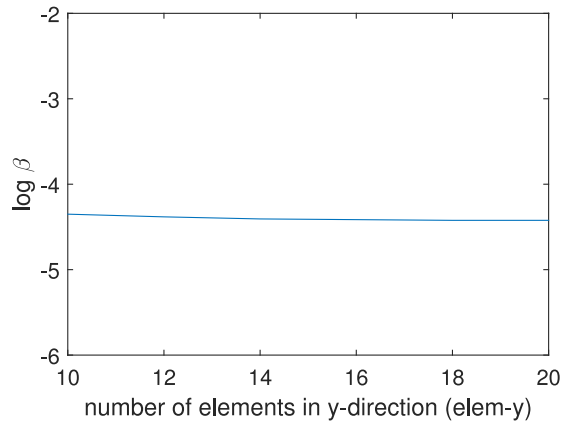


Fig. C.15. Inf-sup constant.

## References

- Abdollahi, A., Arias, I., 2015. Constructive and destructive interplay between piezoelectricity and flexoelectricity in flexural sensors and actuators. *J. Appl. Mech.* 82, 121003.
- Abdollahi, A., Peco, C., Millan, D., Arroyo, M., Arias, I., 2014a. Computational evaluation of the flexoelectric effect in dielectric solids. *J. Appl. Phys.* 116, 093502.
- Abdollahi, A., Millan, D., Peco, C., Arroyo, M., Arias, I., 2015a. Revisiting pyramid compression to quantify flexoelectricity: a three-dimensional simulation study. *Phys. Rev. B* 91, 104103.
- Abdollahi, A., Peco, C., Millan, D., Arroyo, M., Arias, I., 2015b. Fracture toughening and toughness asymmetry induced by flexoelectricity. *Phys. Rev. B* 92, 094101.
- Ahmadpoor, F., Sharma, P., 2015. Flexoelectricity in two-dimensional crystalline and biological membranes. *Nanoscale* 7, 16555–16570.
- Allaire, G., Jouve, F., Toader, A.M., 2004. Structural optimization using sensitivity analysis and a level-set method. *J. Comput. Phys.* 194, 363–393.
- Amanatidou, E., Aravas, N., 2002. Mixed finite element formulations of strain-gradient elasticity problems. *Comput. Methods Appl. Mech. Eng.* 191 (15–16), 1723–1751. [http://dx.doi.org/10.1016/S0045-7825\(01\)00353-X](http://dx.doi.org/10.1016/S0045-7825(01)00353-X).
- Anton, S.R., Sodano, H.A., 2007. A review of power harvesting using piezoelectric materials (2003–2006). *Smart Mater. Struct.* 16, R1–R21.
- Baskaran, S., He, X., Chen, Q., Fu, J.Y., 2011. Experimental studies on the direct flexoelectric effect in  $\alpha$ -phase polyvinylidene fluoride films. *Appl. Phys. Lett.* 98, 242901.
- Bendsoe, M.P., Kikuchi, N., 1988. Generating optimal topologies in structural design using a homogenization method. *Comput. Methods Appl. Mech. Eng.* 71, 197–224.
- Berlincourt, D., Jaffe, H., 1958. Elastic and piezoelectric coefficients of single-crystal barium titanate. *Phys. Rev.* 111, 143–148.
- Bhaskar, U.K., Banerjee, N., Abdollahi, A., Wang, Z., Schlom, D.G., Rijnders, G., Catalan, G., 2015. A flexoelectric microelectromechanical system on silicon. *Nat. Nanotechnol.* 11, 263–267.
- Catalan, G., Lubk, A., Vlooswijk, A.H.G., Snoeck, E., Magen, C., Janssens, A., Rispens, G., Rijnders, G., Blank, D.H.A., Noheda, B., 2011. Flexoelectric rotation of polarization in ferroelectric thin films. *Nat. Mater.* 10, 963–967.
- Catalan, G., Sinnamon, L.J., Gregg, J.M., 2004. The effect of flexoelectricity on the dielectric properties of inhomogeneously strained ferroelectric thin films. *J. Phys.* 16, 2253–2264.
- Chapelle, D., Bathe, K.J., 1993. The inf-sup test. *Struct. Multidiscip. Optim.* 47 (4), 537–545.
- Chen, S., Gonella, S., Chen, W., Liu, W.K., 2010. A level set approach for optimal design of smart energy harvesters. *Comput. Methods Appl. Mech. Eng.* 199, 2532–2543.
- Chu, B., Zhu, W., Li, N., Cross, L.E., 2009. Flexure mode flexoelectric piezoelectric composites. *J. Appl. Phys.* 106, 104109.
- Cross, L.E., 2006. Flexoelectric effects: charge separation in insulating solids subjected to elastic strain gradients. *J. Mater. Sci.* 41, 53–63.
- Dai, S., Gharbi, M., Sharma, P., Park, H.S., 2011. Surface piezoelectricity: size effects in nanostructures and the emergence of piezoelectricity in non-piezoelectric materials. *J. Appl. Phys.* 110, 104305.
- Deaton, J.D., Grandhi, R.V., 2014. A survey of structural and multidisciplinary continuum topology optimization: post 2000. *Struct. Multidiscip. Optim.* 49, 1–38.

- Deng, Q., Kammoun, M., Erturk, A., Sharma, P., 2014a. Nanoscale flexoelectric energy harvesting. *Int. J. Solids Struct.* 51, 3218–3225.
- Deng, Q., Liu, L., Sharma, P., 2014c. Flexoelectricity in soft and biological membranes. *J. Mech. Phys. Solids* 62, 209–227.
- Duerloo, K.-A.N., Reed, E.J., 2013. Flexural electromechanical coupling: a nanoscale emergent property of boron nitride bilayers. *Nano Lett.* 13, 1681–1686.
- Dumitrica, T., Landis, C.M., Yakobson, B.I., 2002. Curvature-induced polarization in carbon nanoshells. *Chem. Phys. Lett.* 360, 182–188.
- Ghasemi, H., Park, H.S., Rabczuk, T., 2017. A level-set based iga formulation for topology optimization of flexoelectric materials. *Comput. Methods Appl. Mech. Eng.* 313, 239–258.
- Hoang, M.-T., Yvonnet, J., Mitrushchenkov, A., Chambaud, G., 2013. First-principles based multiscale model of piezoelectric nanowires with surface effects. *J. Appl. Phys.* 113 (1). <http://dx.doi.org/10.1063/1.4773333>.
- Huang, W., Kim, K., Zhang, S., Yuan, F.G., Jiang, X., 2011. Scaling effect of flexoelectric (ba,sr)tio<sub>3</sub> microcantilevers. *Phys. Status Solidi RRL* 5 (9), 350–352.
- Shu, J.Y., King, W.E., Fleck, N.A., 1999. Finite elements for materials with strain gradient effects. *Int. J. Numer. Methods Eng.* 44, 373–391.
- Jiang, X., Huang, W., Zhang, S., 2013. Flexoelectric nano-generator: materials, structures and devices. *Nano Energy* 2, 1079–1092.
- Kalinin, S.V., Meunier, V., 2008. Electronic flexoelectricity in low-dimensional systems. *Phys. Rev. B* 77, 033403.
- Kogan, S.M., 1964. Piezoelectric effect during inhomogeneous deformation and acoustic scattering of carriers in crystals. *Soviet Phys. Solid State* 5 (10), 2069–2070.
- Krichen, S., Sharma, P., 2016. Flexoelectricity: a perspective on an unusual electromechanical coupling. *J. Appl. Mech.* 83, 030801.
- Li, L., Wang, M.Y., Wei, P., 2012. XFEM schemes for level set based structural optimization. *Front. Mech. Eng.* 7(4), 335–356.
- Liu, C.C., Hu, S.L., Shen, S.P., 2012. Effect of flexoelectricity on electrostatic potential in a bent piezoelectric nanowire. *Smart Mater. Struct.* 21, 115024.
- Liu, L.P., Sharma, P., 2013. Flexoelectricity and thermal fluctuations of lipid bilayer membranes: renormalization of flexoelectric, dielectric, and elastic properties. *Phys. Rev. E* 87, 032715.
- Lu, H., Bark, C.-W., de los Ojos, D.E., Alcalá, J., Eom, C.B., Catalan, G., Gruverman, A., 2012. Mechanical writing of ferroelectric polarization. *Science* 336, 59–61.
- Ma, W., Cross, L.E., 2003. Strain-gradient-induced electric polarization in lead zirconate titanate ceramics. *Appl. Phys. Lett.* 82, 3293–3295.
- Ma, W., Cross, L.E., 2006. Flexoelectricity of barium titanate. *Appl. Phys. Lett.* 88, 232902.
- Majdoub, M.S., Sharma, P., Cagin, T., 2008a. Dramatic enhancement in energy harvesting for a narrow range of dimensions in piezoelectric nanostructures. *Phys. Rev. B* 78, 121407.
- Majdoub, M.S., Sharma, P., Cagin, T., 2008b. Enhanced size-dependent piezoelectricity and elasticity in nanostructures due to the flexoelectric effect. *Phys. Rev. B* 77, 125424.
- Mao, S., Purohit, P.K., 2015. Defects in flexoelectric solids. *J. Mech. Phys. Solids* 84, 95–115.
- Mao, S., Purohit, P.K., Aravas, N., 2016. Mixed finite-element formulations in piezoelectricity and flexoelectricity. *Proc. R. Soc. London A* 472 (2190). doi:10.1098/rspa.2015.0879.
- Maranganti, R., Sharma, N.D., Sharma, P., 2006. Electromechanical coupling in nonpiezoelectric materials due to nanoscale nonlocal size effects: greens function solutions and embedded inclusions. *Phys. Rev. B* 74, 014110.
- Maranganti, R., Sharma, P., 2009. Atomistic determination of flexoelectric properties of crystalline dielectrics. *Phys. Rev. B* 80, 054109.
- Mbarki, R., Baccam, N., Dayal, K., Sharma, P., 2014. Piezoelectricity above the curie temperature? combining flexoelectricity and functional grading to enable high-temperature electromechanical coupling. *Appl. Phys. Lett.* 104, 129204.
- Meyer, R.B., 1969. Piezoelectric effects in liquid crystals. *Phys. Rev. Lett.* 22 (18), 918–921.
- Mohammadi, P., Liu, L.P., Sharma, P., 2014. A theory of flexoelectric membranes and effective properties of heterogeneous membranes. *J. Appl. Mech.* 81, 011007.
- Nanthakumar, S.S., Lahmer, T., Zhuang, X., Park, H.S., Rabczuk, T., 2016. Topology optimization of piezoelectric nanostructures. *J. Mech. Phys. Solids* 94, 316–335.
- Narvaez, J., Vasquez-Sancho, F., Catalan, G., 2016. Enhanced flexoelectric-like response in oxide semiconductors. *Nature* 538 (7624), 219–221.
- Nguyen, T.D., Mao, S., Yeh, Y.-W., Purohit, P.K., McAlpine, M.C., 2013. Nanoscale flexoelectricity. *Adv. Mater.* 25, 946–974.
- Petrov, A.G., 2001. Flexoelectricity of model and living membranes. *Biochim. Biophys. Acta* 1561, 1–25.
- Roundy, S., 2005. On the effectiveness of vibration-based energy harvesting. *J. Intell. Mater. Syst. Struct.* 16, 809–823.
- Rozvany, G.I.N., 2001. Aims, scope, methods, history and unified terminology of computer-aided topology optimization in structural mechanics. *Struct. Multidiscip. Optim.* 21, 90–108.
- Rupp, C.J., Evgrafov, A., Maute, K., Dunn, M.L., 2009. Design of piezoelectric energy harvesting systems: a topology optimization approach based on multi-layer plates and shells. *J. Intell. Mater. Syst. Struct.* 20, 1923–1939.
- Priya, S., Inman, D.J., 2009. *Energy Harvesting Technologies*. Springer.
- Saber, A., Mansouri, K., Renard, Y., Arfaoui, M., Moakher, M., 2011. Numerical convergence and stability of mixed formulation with x-fem cut-off. 10e colloque national en calcul des structures.
- Sharma, N.D., Landis, C.M., Sharma, P., 2010. Piezoelectric thin-film superlattices without using piezoelectric materials. *J. Appl. Phys.* 108 (2). doi:10.1063/1.3443404.
- Sharma, N.D., Maranganti, R., Sharma, P., 2007. On the possibility of piezoelectric nanocomposites without using piezoelectric materials. *J. Mech. Phys. Solids* 55, 2328–2350.
- Shen, S., Hu, S., 2010. A theory of flexoelectricity with surface effect for elastic dielectrics. *J. Mech. Phys. Solids* 58, 665–677.
- Sigmund, O., Maute, K., 2013. Topology optimization approaches. *Struct. Multidiscip. Optim.* 48, 1031–1055.
- Silva, E.C.N., Kikuchi, N., 1999. Design of piezoelectric transducers using topology optimization. *Smart Mater. Struct.* 8, 350–364.
- Priya, S., 2007. Advances in energy harvesting using low profile piezoelectric transducers. *J. Electroceram.* 19, 167–184.
- Stengel, M., 2013. Flexoelectricity from density-functional perturbation theory. *Phys. Rev. B* 88, 174106.
- Tagantsev, A.K., 1986. Piezoelectricity and flexoelectricity in crystalline dielectrics. *Phys. Rev. B* 34 (8), 5883–5889.
- Todorov, A.T., Petrov, A.G., Fendler, J.H., 1994. First observation of the converse flexoelectric effect in bilayer lipid membranes. *J. Phys. Chem.* 98, 3076–3079.
- Wendland, H., 1995. Piecewise polynomial, positive definite and compactly supported radial functions of minimal degree. *Adv. Comput. Math.* 4.1, 389–396.
- Yan, Z., Jiang, L.Y., 2013. Flexoelectric effect on the electroelastic responses of bending piezoelectric nanobeams. *J. Appl. Phys.* 113, 194102.
- Yang, W., Liang, X., Shen, S., 2015. Electromechanical responses of piezoelectric nanoplates with flexoelectricity. *Acta Mech.* 226, 3097–3110.
- Yudin, P.V., Tagantsev, A.K., 2013. Fundamentals of flexoelectricity in solids. *Nanotechnology* 24, 432001.
- Yvonnet, J., Liu, L.P., 2017. A numerical framework for modeling flexoelectricity and maxwell stress in soft dielectrics at finite strains. *Comput. Methods Appl. Mech. Eng.* 313, 450–482.
- Zheng, B., Chang, C., Gea, H., 2009a. Topology optimization of energy harvesting devices using piezoelectric materials. *Struct. Multidiscip. Optim.* 38 (1), 17–23.
- Zheng, B., Chang, C.-J., Gea, H.C., 2009b. Topology optimization of energy harvesting devices using piezoelectric materials. *Struct. Multidiscip. Optim.* 38, 17–23.
- Zhu, W., Fu, J.Y., Li, N., Cross, L., 2006. Piezoelectric composite based on the enhanced flexoelectric effects. *Appl. Phys. Lett.* 89, 192904.
- Zubko, P., Catalan, G., Tagantsev, A.K., 2013. Flexoelectric effect in solids. *Annu. Rev. Mater. Res.* 43, 387–421.